RSC Advances

PAPER

View Article Online
View Journal | View Issue

Cite this: *RSC Adv.*, 2026, **16**, 332

Influence of pseudohalide anions on non-covalent supramolecular synthons in Hg(II) complexes with an 8-aminoquinoline ligand: DFT approach and biological implications

Dhrubajyoti Majumdar, *[a] Antonio Frontera, *[b] Jessica Elizabeth Philip,[c] Bouzid Gassoumi,[d] Sergi Burguera,[b] Sourav Roy[e] and Sahbi Ayachi[f]

In this work, we report the synthesis, structural characterization, DFT calculations, and antimicrobial/anticancer properties of two identical X-ray structures of Hg(II) complexes (**1** and **2**). The complexes crystallized in the monoclinic space group $P2_1/c$. Hg(II) ions in two complexes exhibit four-coordinated geometries. The complex crystal network flourishes with hydrogen bonds and π···π interactions. In the crystal networks, supramolecular features have been explained by Hirshfeld surface and 2D fingerprint plots. The HOMO–LUMO energy gap of Hg(II) complexes enables conducting behaviour. NLO examines complex **2**, which is a promising candidate for optoelectronic applications. The NLO findings are in accordance with the calculated hyperpolarizability (β_0) values. Further, X-ray structure reveals the existence of spodium (SpB) and chalcogen bonds (ChB) in the crystal networks of the complexes. QTAIM, NCI-RDG plots, NBO, and MEP studies successfully ensure the existence of these bonds. Also, energy decomposition analysis (EDA) rationalizes the role of electrostatics in all cases. Here, it is highlighted that dispersion plays a vital role in dimers showing LP···π interactions. However, in the case of hydrogen-bonding, the orbital effects are equally significant. Meanwhile, the as-prepared compounds' antimicrobial activities were investigated against Gram-positive and Gram-negative microbial strains. These studies include *S. aureus* (ATCC 25923) and *B. subtilis* (ATCC 6633), *E. coli* (ATCC 25922) and *S. typhimurium* (ATCC 14028), the fungus *A. fumigatus*, and the yeast *C. albicans* (ATCC 10231). The MIC value compares the antimicrobial results. Additionally, cytotoxicity was assessed in DLA, HepG2, and human H9c2 cancer cell lines, revealing that Hg(II) complexes exhibit low cytotoxicity in human H9c2 cells. The structure–activity relationship (SAR) rationalized the core biological findings.

Received 9th December 2025
Accepted 15th December 2025

DOI: 10.1039/d5ra09546h

rsc.li/rsc-advances

1. Introduction

The coordination chemistry with the N-containing heterocycle ligand began with Blau's research input after synthesizing transition metal complexes in contact with *N*-donor 2,2′-bipyridine.[1,2] Various heterocyclic metal complexes have been studied under this venture, demonstrating their structural advancements and exhibiting chemical, electrochemical, photophysical, photochemical, and catalytic properties.[2–5] Consequently, *N*,*N*-donor 8-aminoquinoline (8-aq) is a chelating ligand, exploring coordination number 4 complexes with Hg(II) or other metal ions in synthetic coordination chemistry. The 8-aq synthesized compounds are a well-researched heteroaromatic system due to their antiprotozoal and versatile medicinal properties.[6,7] Notably, in the 8-aq ligand, the structural integrity of the quinoline moiety (*q*) (Scheme S1)[8] attracts synthetic researchers owing to its versatile coordination behaviour and unique supramolecular properties, leading to applications in catalysis, materials chemistry, lanthanide sensing, organic synthesis, medicinal chemistry, and electrochemistry.[8,9] In addition, the 8-aq was selected due to its intriguing fluorescent and pharmaceutical (pH) properties.[10–12] There are a few instances of Zn/Cd/Mn/Ni/Fe complexes with 8-aq ligands in the Cambridge Structural Database (CSD).[13,14] However, examples of Hg(II) complexes with 8-aq and pseudohalides SCN^-/$SeCN^-$ are rare in the literature.[2,15–21]

[a]*Department of Chemistry, Tamralipta Mahavidyalaya, Tamluk 721636, West Bengal, India. E-mail: dmajumdar30@gmail.com*

[b]*Department de Quimica, Universitat de Les Illes Balears, Crta. de Valldemossa km 7.5, 07122, Palma de Mallorca, Baleares, Spain. E-mail: toni.frontera@uib.es*

[c]*Department of Chemistry, St. George's College, Aruvithura, Kottayam, Kerala, 686122, India*

[d]*Laboratory of Advanced Materials and Interfaces (LIMA), Faculty of Sciences of Monastir, Avenue of Environment, University of Monastir, 5000 Monastir, Tunisia*

[e]*Solid State and Structural Chemistry Unit, Indian Institute of Science, Bangalore, 560 012, India*

[f]*Laboratory of Physico-Chemistry of Materials (LR01ES19), Faculty of Sciences, University of Monastir, Avenue of the Environment, 5019 Monastir, Tunisia*

Pseudohalides such as $SCN^-/SeCN^-$ are highly demanding ambidentate spacers in coordination chemistry for constructing metal–complex crystal networks with different dimensions.[22–31] To date, Hg(II) complexes with these pseudohalides are scant in the literature.[2,15–21,32] Meanwhile, in the 20th century, the field of coordination chemistry shifted its focus to noncovalent interactions (NCIs), including (H/halogen/π-interactions: π···π, CH···π, CO···π, and ion···π), which are now well researched.[33–35] Scientists have identified various NCI with d-block elements in recent years, covering Regium (Group 11), SpBs (spodium) (Group 12), and Osme bonds (Group 8).[35] The SpB interaction occurs between a Group 12 metal and a L^{eRICH} (electron-rich), and the nature of these bonds is opposite to the classical coordination bond.[35] In this context, X. Zhang *et al.* examine Bauza *et al.*'s work which demonstrated through CSD and DFT calculations that a σ-hole region exists in the MX_2L_2 complexes (M = Zn/Cd/Hg), facilitating noncovalent interactions.[35] Furthermore, in biological systems, few Hg(II) complexes effectively donate SpBs, helping in the approach of L^{eRICH} metals,[35] and also, the Hg···N bond is crucial for the existence of supramolecular features in Hg(II) complexes, *viz*, $[Hg(HL)(SCN)_2]$.[35] Both interactions can reinforce each other in metal complexes with a SpBs/Pnicogen/Tetrel bond, which is crucial for designing metal complexes within the crystal engineering community.[35–37] Group 12 metal Hg(II) complexes with π-hole/σ-hole donor character are limited in the literature. Similarly, X. Zhang extended the work of Mahmoudi *et al.*, who recently synthesized and characterized π-hole SpBs in complexes such as $[Hg(L^I)I]_n$ and $[Hg(HL^{II})I_2]$.[35] Therefore, the coordination and structural chemistry of Hg(II) halides with 8-aq containing various donor atoms and pseudohalides has generated considerable research interest.[15] Meanwhile, current research has utilized comprehensive DFT tools (MEP, QTAIM, NCI-RDG plot, NBO) to analyse these bonding features in Hg(II) complexes.[38,39] In continuation of our long-term research interests, the antimicrobial and cytotoxicity of Hg(II) complexes with 8-aq against cancer cell lines (DLA, HepG2, and human H9c20) is another milestone in novel research, as it is, to date, limited in the literature.[40]

Herein, we report the synthesis, characterization, and X-ray structure of two isostructural Hg(II) complexes in contact with 8-aq and pseudohalides. The article explores noncovalent interactions in the crystal network of Hg(II) complexes formed by $SCN^-/SeCN^-$ spacers. The role of noncovalent interactions in solid-state crystal assembly has been rationalized through a panel of DFT studies (MEP surfaces, QTAIM, NCI-RDG plots, NBO, and EDA). The antimicrobial and anticancer properties of Hg(II) complexes were investigated, along with their structure–activity relationships, thereby articulating the key findings of the biological research.

2. Experimental section

2.1. Materials

The current research used AR-grade chemicals and solvents without additional purification. $HgCl_2$, 8-aminoquinoline (8-aq), NaSCN, and KSeCN (potassium selenocyanate) were purchased from Sigma Aldrich. Methanol (CH_3OH) and dichloromethane (DCM) solvents were obtained from TCI, America.

2.2. Physical measurements

The CHN was analysed using a PerkinElmer 2400 CHN elemental instrument. The Xevo G2-XS QToF 4 K instrumental model was used to measure HRMS. PerkinElmer and Bruker RFS 27 modes were used for IR and Raman spectroscopy (400–4500 cm^{-1}). Bruker FT-NMR spectrometer analysed NMR in DMSO-d_6 solvents. The Oxford XMX N model was used for EDX analysis and various SEM images with a JEOL JSM-6390LV model. Hitachi U-3501 model measures UV-visible spectra at wavelengths 200–800 nm. The Thermo-Scientific NEXA model analysed the XPS spectrum, including scans for N 1s, C 1s, Cl 2p, S 2p, and Hg 4f.

2.3. Synthesis of Hg(II) complexes

2.3.1. [Hg{(8-aq) (SCN)Cl}] 1. Initially, in a mortar, 0.271 g of $HgCl_2$ (1 mmol) and 0.144 g of 8-aq (1 mmol) were ground with a pestle for about 5 minutes. Then, the overall white colour solid mixture was poured into a solvent mixture of 20 mL CH_3OH and DCM (1 : 1 molar ratio) after refluxing for 15 minutes at ambient temperature. Then, a few drops of a methanol solution of NaSCN (0.081 g, 1 mmol) were added and mixed after shaking in a mechanical shaker for three minutes. The final solution was stirred using a magnetic stirrer for 1 hour. The cooled, light-yellow solution was filtered and slowly evaporated for crystallization. After a few days, suitable single crystals for SCXRD were collected and air-dried. Yield: 202.30 mg (49.8%). Anal. calc. for $C_{10}H_8ClHgN_3S$: C, 27.40; H, 1.84; N, 9.59, found: C, 27.37; H, 1.79; N, 9.62, HRMS for complex **1**, (*m*/*z*, TOF MS): found for 438.29 (calculated 439.8), for complex **1**, *ν*(N–H), 3481, *ν*(C=C), 1617, *ν*(phenyl ring), 1468, 1370, *ν*(SCN), 2105, FT-Raman (cm^{-1}) selected bands: *ν*(C=C), 1615 s, *ν*(phenyl ring), 1392 s, *ν*(Hg–N), 575 s, *ν*(C–N–Hg), 992, 1250 m, *ν*(SCN), 2120 s, ^{1}H NMR (DMSO-d_6, 400 MHz): *δ* (ppm): for complex **1**, 8.73 (1H, br, s), 8.19 (1H, d, $J = 8.0$ Hz), 7.46 (1H, m), 7.30 (1H, t, $J = 8.0$ Hz), 7.10 (1H, d, $J = 8.0$ Hz), 6.91 (1H, d, $J = 7.2$ Hz), 6.01 (2H, br, s), and ^{13}C NMR (DMSO-d_6, 400 MHz): *δ* (ppm): 109.41–127.47 (C Ar), 135.91–147.04 (C Ar), ^{13}C DEPT NMR: *δ* (ppm): 108.58–128.40 (C Ar), 136.33–147.73 ppm (C Ar), UV-Vis λ_{max} (DMF): 265 nm (ε = 42.80 M^{-1} cm^{-1}), and 344 nm (ε = 15.44 M^{-1} cm^{-1}).

2.3.2. [Hg{(8-aq) (SeCN)Cl}] 2. We used identical synthetic methods to synthesize complex **2**, using 0.271 g of $HgCl_2$ (1 mmol), 0.144 g of 8-aq (1 mmol), and a few drops of a methanol solution of KSeCN (0.144 g, 1 mmol) instead of NaSCN. Yield: 241.14 mg (49.8%). Anal. calc. for $C_{10}H_8ClHgN_3Se$: C, 24.75; H, 1.66; N, 8.66, found: C, 131; H, 1.70; N, 8.70, HRMS for complex **2**, (*m*/*z*, TOF MS): found for 485.19 (calculated 486.10), for complex **2**, *ν*(N–H), 3220, *ν*(C=C), 1615, *ν*(phenyl ring), 1470, 1369, *ν*(SeCN), 2127 s, FT-Raman (cm^{-1}) selected bands: *ν*(C=C), 1610 s, *ν*(phenyl ring), 1383 s, *ν*(Hg–N), 552 s, *ν*(C–N–Hg), 1282 m, *ν*(SeCN), 2136 s, ^{1}H NMR (DMSO-d_6, 400 MHz): *δ* (ppm): for complex **2**, 8.73 (1H, d, $J = 4$, 1.6 Hz), 8.19 (1H, dd, $J = 8.4$, 2

Hz), 7.47 (1H, dd, $J = 8.4$, 4.0 Hz), 7.31 (1H, t, $J = 7.6$ Hz), 7.11 (1H, d, $J = 8.4$ Hz), 6.92 (1H, dd, $J = 7.6$, 1.2 Hz), 6.05 (2H, br, s), and ^{13}C NMR (DMSO-d_6, 75.45 MHz): δ (ppm):109.71–128.54 (C Ar), 136.03–147.15 (C Ar), ^{13}C DEPT NMR: δ (ppm): 110.76–128.40 (C Ar), 137.22–147.32 ppm (C Ar), UV-Vis λ_{max} (DMF): 273 nm ($\varepsilon = 56.40$ M^{-1} cm^{-1}).

2.4. X-ray crystallography

Table S1 presents the crystallographic data and structure refinement parameters. The crystallographic data were collected at a temperature between 296.15 and 298(2) K. The high-quality crystal growth was achieved by slowly evaporating CH_3OH + DCM solvent mixtures. The crystal data were collected using a Bruker-AXS SMART APEX II diffractometer, employing standard Mo Kα radiation ($\lambda = 0.71073$ Å). The crystal structures were solved using different crystallographic software programs, including the advanced SHELX,[41] SADABS,[41] and SAINT.[41] The crystal space group (SG), structure, and F^2 were accurately determined using SHELXTL and least-squares methods. Full-matrix least-squares methods and refinement using SHELXL-2014,[41] and Olex-2 software[41] ultimately solved the complex's structure. The crystal structure was refined by applying anisotropic shift parameters to all atoms, with the H atoms refined iso-tropically.

2.5. Computational methods

The Hg(II) complex CIF file has been optimized using the DFT/B3LYP-D3/LanL2DZ method[42–46] implemented in the Gaussian 09 package.[47] Relativistic contributions for the Hg(II) center were treated using effective core potentials (LanL2DZ), which replace the inner core electrons with an effective potential and thus incorporate the dominant relativistic effects efficiently. Energetic refinements at the PBE0-D4/def2-TZVP level further ensured reliable electronic descriptions. Although spin–orbit coupling was not explicitly included, this ECP-based framework is well established for providing accurate structures and electronic properties of Hg(II) complexes. The FMO was conducted to investigate the electronic properties and the donor (D)/acceptor (A) characteristics of Hg(II) compounds.[48] The Electron Localization Function (ELF) and Localized Orbital Locator (LOL) are utilized to analyse the electronic distribution on the surface of the materials.[49] Furthermore, the Turbomole program 7.7 (ref. 50) at the PBE0-D4/def2-TZVP level of theory[51–54a] was used to perform the energetic calculations. This functional has been selected since it provides good estimates of both geometries and energies for Hg(II) compounds.[54b,c] The geometries of the complexes studied herein were obtained from X-ray coordinates. We then performed a geometry optimization where only the hydrogen atom positions were optimized, while the heavy atoms were kept fixed at their experimental positions. This approach was chosen to analyse the intermolecular interactions as they exist in the solid state, rather than optimizing the entire structure to its lowest-energy gas-phase conformation. An iso-surface of 0.001 au was used for plotting the MEP surface, which were represented using Gaussview 6.0 program.[54d] Using the VMD software,[55] QTAIM[56]/NCI Plot[57] analyses were computed. The Multiwfn program[58] is recommended for the QTAIM/NCI plot calculations. The NBO analysis was performed using the NBO7 program.[59] Employing the Kitaura–Morokuma scheme,[60] the EDA calculations were performed using the Turbomole 7.7 program. Dimerization energies were obtained directly from the EDA based on the defined monomer fragments.

2.6. Biological studies

2.6.1. Disc diffusion method. The antibacterial potency of the synthesized Hg(II) complexes was evaluated against Gram-positive bacteria, including *S. aureus* (ATCC 25923) and *B. subtilis* (ATCC 6633), as well as Gram-negative bacteria such as *E. coli* (ATCC 25922) and *S. typhimurium* (ATCC 14028). Similarly, the antifungal efficacy of *C. albicans* (ATCC 10231) and *A. fumigatus* was considered in the current study. The analysis was conducted using the disc diffusion method (DDM).[61,62] Cephalothin, chloramphenicol, and cycloheximide were used as positive controls for Gram-positive and Gram-negative bacteria and fungi. The detailed antimicrobial experimental protocol is submitted in Section S1.

2.6.2. Minimum inhibitory concentration (MIC)-resazurin based microtiter dilution assay (RMDA). The antimicrobial efficacy of investigated mercury compounds was assessed using the Resazurin Microdilution Assay (RMDA).[62] All the experiments were taken in triplicate, and the average MIC values for each test compound were calculated.[63,64] A detailed experimental protocol is submitted in Section S2.

2.6.3. Cytotoxicity and MTT assay. Hg(II) complexes *in vitro* cytotoxicity was examined on HepG-2 and H9c2 cell lines. H9c2 cells (embryonic BD1X rat heart tissue) were provided by the National Centre for Cell Sciences (NCCS), Pune, India, and cultured in Dulbecco's modified Eagle's medium (DMEM) with 10% FBS, penicillin (100 U mL^{-1}), and streptomycin (100 mg mL^{-1}) at 37 °C under a 5% CO_2 atmosphere. Cells were subcultured to 80% confluence before experiments. Similarly, the HepG2 human hepatocellular carcinoma cell line was also obtained from previous sources, NCCS and maintained in Eagle's minimum essential medium with 10% FBS, penicillin (100 U mL^{-1}), and streptomycin (100 mg mL^{-1}) under a 5% CO_2 environment at 37 °C, with subculturing to 80% confluence before use.[65,66] The MTT assay (3-(4,5-dimethylthiazol-2-yl)-2,5-diphenyltetrazolium bromide) was sourced from Sigma, St Louis, MO, USA (Section S3 for experimental details). The percentage (%) cell viability of control cells was kept at 100%. The retained cells in percent were determined based on the given formula:

$$\%\ \text{Cell viability} = \left(100 - \frac{\text{absorbance of treated}}{\text{absorbance of control}}\right) \times 100$$

2.6.4. Trypan blue exclusion assay. The cell viability was examined using the Trypan blue exclusion method (TBEM)[66] with a standard experimental protocol after dissolving multiple concentrations of Hg(II) compounds in DMSO. The complexes were kept at 37 °C for 3 hours. Furthermore, after incubation,

0.1 mL of 1% Trypan blue was added and incubated for 3 minutes before being loaded onto a hemacytometer. Regarding the reference experiments, we observed two distinct outcomes: dead cells took up the blue dye, whereas live cells remained unstained. Stained (that means dead) and unstained (which means life) cells were counted in a stepwise manner, and the % cytotoxicity was calculated based on the given formula.[67]

$$\%\ \text{Cytotoxicity} = \left(\frac{\text{number of dead cells}}{\text{number of live cells} + \text{number of dead cells}}\right) \times 100$$

3. Results and discussion

Two water-insoluble iso-structural Hg(II) complexes were synthesized using 8-aq chelating ligand and pseudohalides *via* a self-assembly *in situ* technique (Scheme 1). Different analytical methods are employed to characterize the complexes, including SEM-EDX and X-ray photoelectron spectroscopy (XPS). The Hg(II) complexes with 8-aq and pseudohalide coordination chemistry are scarce in the literature,[2,15–21,32] especially for noncovalent interactions (NCI), which encompass SpBs/σ/π holes within the crystal networks. Notably, DFT methods, including MEP, QTAIM, NCI-RDG plots, NBO, and EDA, are widely used to investigate the nature of NCI in Hg(II) complexes. Similarly, the combined antimicrobial and antiproliferative activities against cancer cell lines (DLA, HepG2, and human H9c2) is scarce for Hg(II) complexes. The distinctive supramolecular characteristics of crystal assemblies, SpB/σ/π-hole bond concepts, and their significance in biology underscore the originality of metal complexes research.

4. Characterization

Hg(II) complexes are well characterized structurally using a variety of analytical methods.

4.1. HRMS

Hg(II) complexes' structural integrity was confirmed by HRMS characterization (Fig. S1 and S2). The complex molecular ion peaks were observed at 439.84 *m*/*z* (calculated 438.29, **1**) and 486.10 *m*/*z* (calculated 485.19, **2**), confirming the Hg(II) complexes' stoichiometry in the presence of pseudohalides.

4.2. IR and Raman spectroscopy

The Hg(II) complexes were primarily characterized using IR and Raman spectroscopic studies (Fig. S3a–c, S4a, b, S5a and b). In **1** & **2**, these stretching band-shifted values are identified at 3481, 1617, 1468, and 1370 cm^{-1} (**1**) and 3220, 1615, 1470, and 1369 cm^{-1} (**2**), respectively. These IR shifting values confirm that the 8-aq structural framework is present in the complexes, and the 8-aq *N*,*N*-donor centres are coordinated to the Hg(II) centre. The most significant identification of the complexes is the presence of SCN^- (**1**) and $SeCN^-$ (**2**). To prepare the complexes, we used NaSCN and KSeCN salts. Therefore, IR spectroscopy of standard NaSCN and KSeCN salts (Fig. S3a–c) was compared with those of the Hg(II) complexes. The shifting peaks of the complexes at 2105 and 2127 cm^{-1} confirm the presence of the spacer SCN^- and $SeCN^-$ ion in the complexes.[22,28] Furthermore, Raman sharp peak values at 2120 and 2136 cm^{-1} ensure the presence of these spacers in **1** and **2**. In this context, the studied molecular structure of two Hg(II) complexes corresponds to a true minimum, as evidenced by our vibrational frequency calculations, which yield no imaginary frequencies. We have submitted the figure in the SI (Fig. S5c).

4.3. UV-Vis spectrum

The UV-Vis spectra of Hg(II) complexes were analysed using DMF (Fig. S6a–a1/S6b–b1). The UV broad peaks are observed at 265 and 344 nm (**1**) and 273 nm (**2**). The results indicate that the 8-aq interacts with Hg(II) through N-donor atoms, which can be ascribed to a transition involving the π → π* aromatic benzene ring.[68,69] The Hg(II) possesses a $5d^{10}$ filled electronic arrangement, and the HOMO–LUMO orbitals of the complexes are spread out across the QM (quinoline moiety). The properties of the HOMO–LUMO orbitals of the individual quinoline (*q*) unit remain consistent under the given conditions. The complexes electronic transition is like other d^{10} metal complexes.[70] Fig. S6a1–b1 show the additional lower dilution (0.001 M) UV-Vis spectrum.

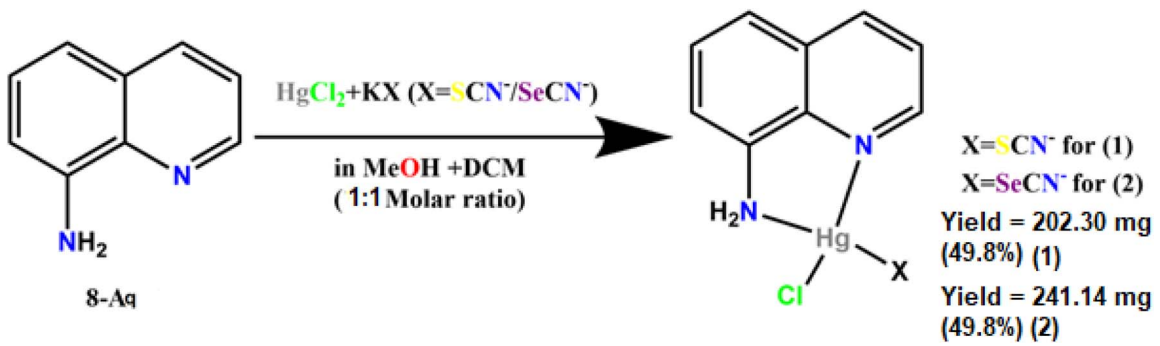

Scheme 1 Synthetic outline for Hg(II) complexes.

4.4. NMR analysis

NMR Fig. S7a–c are applicable for 8-aq, and complex **1** and **2**. The 8-aq NMR studies show significant shifts in the NMR peaks for the Hg(II) complexes. For **1**, the Ar CH proton shifts in nature to δ 6.91–7.46 and δ 8.19 ppm. In contrast, for **2**, the Ar CH shifts are observed at δ 6.92–7.47 and δ 8.19 ppm.[68–70] ^{1}H NMR peak values confirm that Hg(II) complexes contain an aromatic ring coordinated to 8-aq *N*,*N*-donor centres. In addition, a high δ 6.01–6.05 ppm value of the NH_2 proton is seen in both complexes due to the reduction of the electron density during Hg(II) metal coordination with NH_2. The shifting of ^{13}C NMR peak values further substantiates the existence of both complexes' aromatic carbon structural frames (peak shifts at δ: 109.41–127.47 and 135.91–147.04 ppm (**1**), 109.71–128.54 and 136.03–147.15 ppm (**2**) (Fig. S8a and b)). We also assess the aromatic carbon structural integrity of the complexes using ^{13}C ~ DEPT NMR (Fig. S9a and b). In both complexes, we observed similar DEPT NMR peak values covering 108.58–128.40, 136.33–147.73 ppm for **1**, and 110.76–128.40, 137.22–147.32 ppm for **2**.[71]

4.5. EDX-SEM

The SEM is commonly used as a sophisticated technique to analyse the structural morphology and size of Hg(II) complexes.[72] On the other hand, EDX analysis involves using X-rays to map the elemental composition of newly synthesized Hg(II) compounds. The complexes' EDX mapping (Fig. S10) shows their elemental and metal composition, as well as the electron image. EDX mapping concluded that **1** is composed of carbon (C), nitrogen (N), sulphur (S), and mercury (Hg). The EDX suggests the % weight information of the complex (Table S4). EDX mapping confirms the interaction between Hg(II) ions and the 8-aq in the presence of SCN^- ions. SEM micrographs (Fig. S11a–e) confirm that the **1** surface structure resembled an organized ice type. For **1**, SEM micrographs divulge the ice-type morphology. The literature study investigated significant variations in particle size and shape compared to other quinoline-based metal complexes.[70]

4.6. X-ray photoelectron spectroscopy

X-ray photoelectron spectroscopy (XPS) is becoming more significant for mapping the elemental composition and elucidating the formation of Hg(II) complexes in the presence of 8-aq and SCN^- (Fig. S12a–e). XPS studies enhance the interactions between the 8-aq and Hg(II) metal during complex formation. The XPS scan of the binding energy (BE) spectrum provides evidence of N, C, Cl, S, and Hg(II) in **1**. Notably, in **1**, bonding features involving Hg–N, Hg–S, and Hg–Cl are observed. Therefore, the XPS scan image of **1** revealed BE corresponding to the N 1s, C 1s, Cl 2p, S 2p, and Hg 4f peaks: 398.5, 284.7, 198.3, 163.4, 101.2, and 105.1 eV, respectively. Hence, the Hg 4f scan reveals that Hg is in the (II) state, and no elemental Hg is present in **1**, as confirmed by the absence of Hg 4f, which has a binding energy of 99.8 eV.[73] The XPS scan image in **1** also ensures that Hg(II) is the central metal ion. The 284.7 eV C 1s XPS peak in **1** is assigned to the C atoms present in the C–C bond framework.[73,74] Similarly, the N 1s and Cl 2p XPS spectrum's peaks, at 398.5 and 198.3 eV for 1 eV, are associated with the N for SCN^-[33] and Hg–Cl bond formation in the complex.[73] Notably, the Hg–SCN bonding section is present in **1**, as confirmed by the S 2p XPS scan at 163.4 eV.[75a] Finally, in **1**, the most significant bonding features are Hg–SCN (S-bonded), Hg–N (8-aq), and Hg–Cl, as determined by XPS scanning.

5. Crystal structure description

Pseudohalide-linked Hg(II) complexes are isostructural and crystallize in a monoclinic space group $P2_1/c$. In both complexes, the two nitrogen atoms of the aminopyridine ligand behave as donor atoms to bind with the Hg(II) atom, forming a Hg(II)-ligand complex. Each complex's Hg(1) centre is tetra-coordinated, forming distorted tetrahedral geometry. Two nitrogen atoms, [pyridine nitrogen, N(2) and amine nitrogen, N(1)], one chlorine atom, Cl(1), and one sulphur/selenium atom, S(1)/Se(1), are attached with the central Hg(1) to fulfil its coordination geometry (Fig. 1). The bond angles around Hg(1) range from 73.7(3) ° [complex **1**], 73.3(3) ° [complex **2**], to

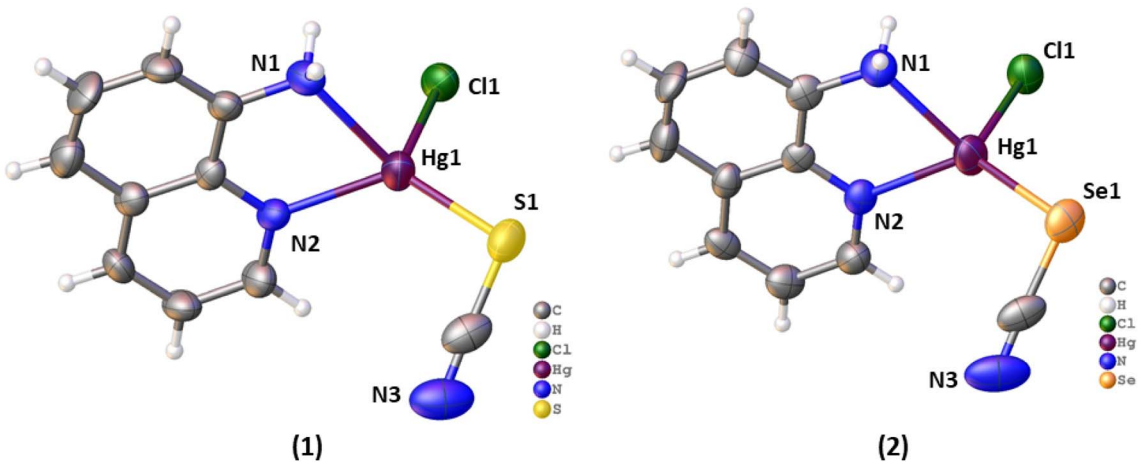

Fig. 1 Perspective view of complexes **1** (left) and **2** (right) with selective atom numbering scheme, (ORTEP ellipsoid probability 50%).

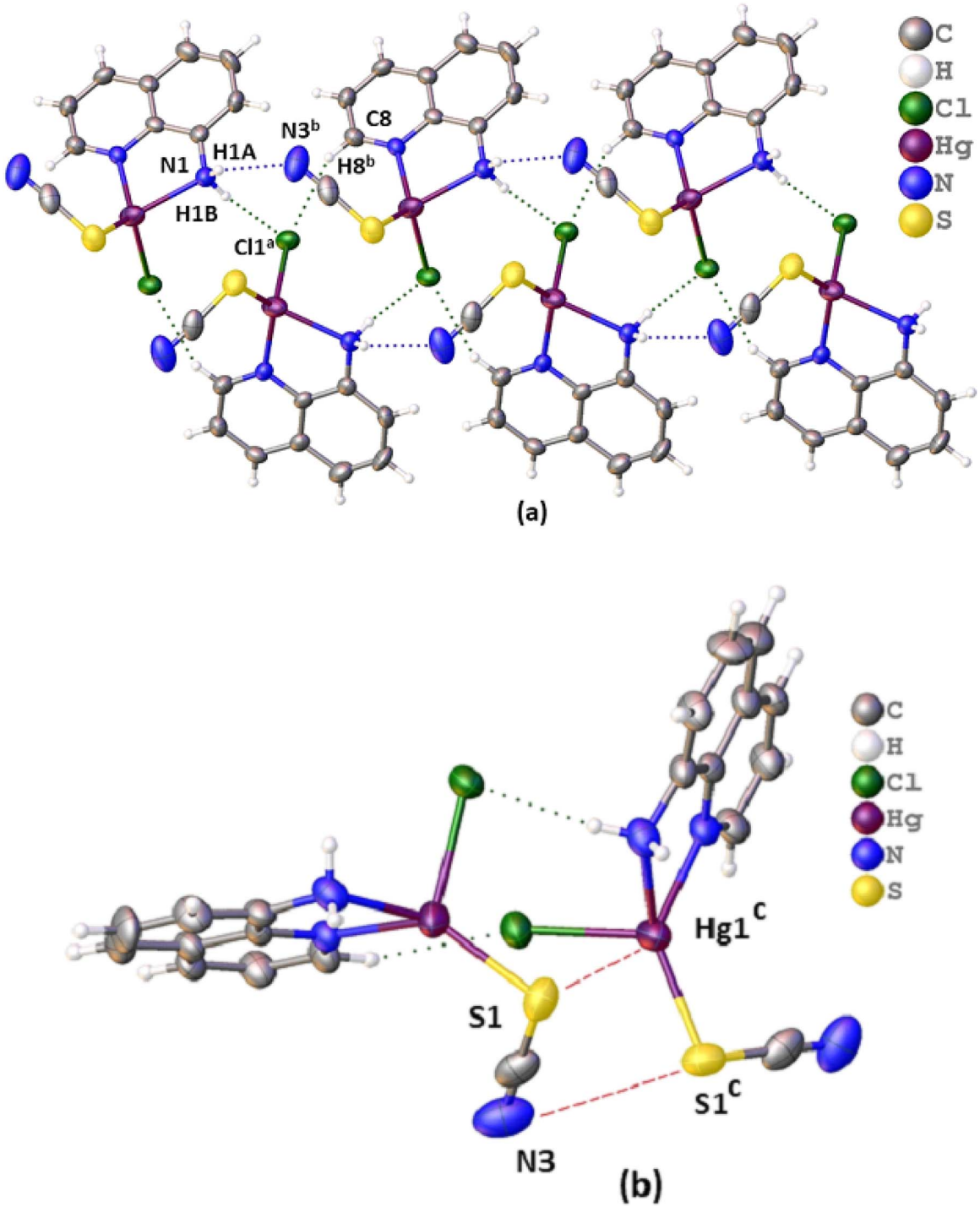

Fig. 2 (a) Perspective view of hydrogen bonding interaction with selective atom numbering scheme. Symmetry operation: $a = x, 1/2 - y, 1/2 + z$, $b = x, y, 1 + z$, $c = x, 1/2 - y, -1/2 + z$, (b) perspective view of Hg···S and S···N contacts observed in **1**.

131.48(19) ° [complex **1**], 131.7(2) ° [complex **2**], indicating that the geometry is significantly distorted. Complete crystallographic parameters are gathered in Table S1.

5.1. Supramolecular interactions

The isostructural Hg(II) complexes exhibit both strong and weak hydrogen bonds in their crystal packing. The hydrogen atom, H1A, attached to N1, forms a symmetry-related (x, y, $1 + z$) hydrogen bond with the thiocyanate nitrogen, N3 in **1**, and the SeCN nitrogen, N3 in **2**. The other amine hydrogen, H1B, attached to N1, forms a symmetry-related (x, $1/2 - y$, $1/2 + z$) hydrogen bond with the chlorine atom, Cl1, in both complexes. Additionally, another hydrogen atom, H8, attached to a carbon atom, C8, forms a symmetry-related (x, $1/2 - y$, $1/2 + z$) hydrogen

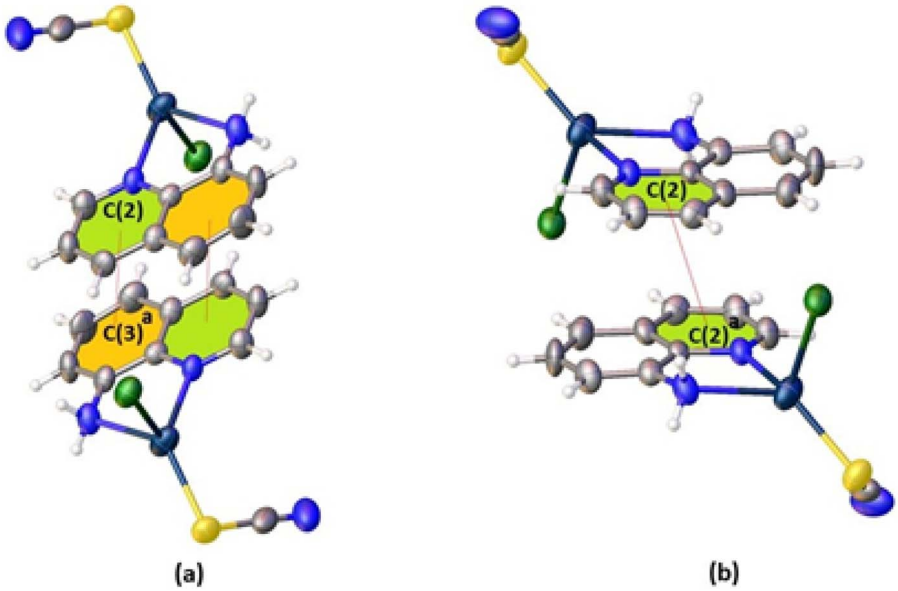

Fig. 3 (a and b) Perspective view of pi···pi interactions in complex **1** with selective atom numbering scheme.

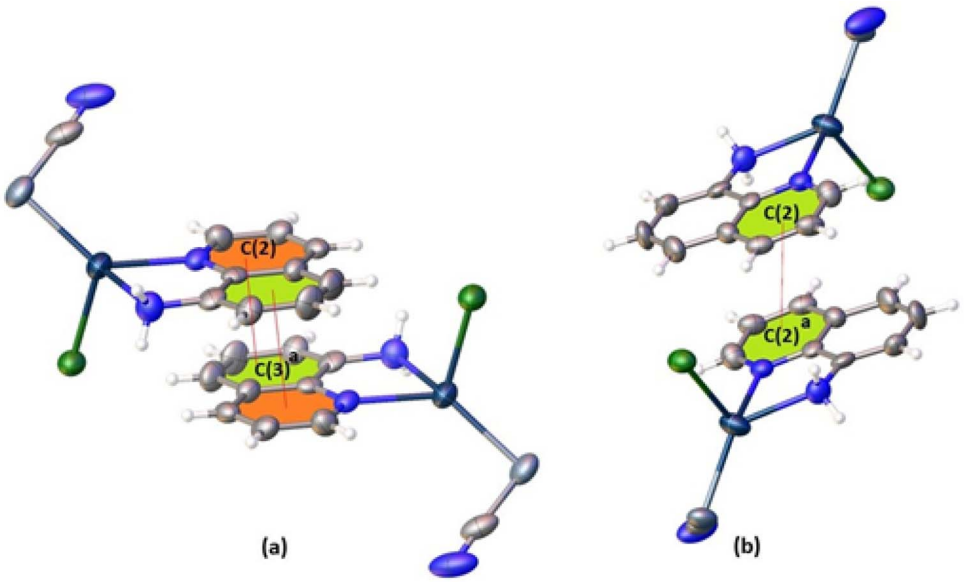

Fig. 4 (a and b) Perspective view of pi···pi interactions in complex **2** with selective atom numbering scheme.

bond with the chlorine atom, Cl1, in both complexes. These interactions lead to the formation of 1-D chains in both complexes, as shown in Fig. 2a. The hydrogen bonding parameters for both complexes are summarised in Table S3. Furthermore, a comparable pattern of π···π interactions is observed in both Hg(II) complexes. In each case, the quinolone ring engages in π···π stacking with the quinolone ring of a neighbouring molecule. Additionally, the pyridine ring [N(2)–C(8)–C(7)–C(6)–C(5)–C(9)] in both complexes exhibits π···π interactions with a symmetry-related phenyl ring [C(1)–C(2)–C(3)–C(4)–C(5)–C(6)] defined by the $(2 - x, 1 - y, 1 - z)$ symmetry operation, as illustrated in Fig. 3a and b. The same pyridine ring also participates in symmetry-related $(2 - x, 1 - y, 1 - z)$ π···π interactions with the pyridine ring of an adjacent molecule in both complexes (Fig. 4a and b). The geometric parameters associated with these interactions are summarized in Table 1. Besides hydrogen bonds, both complexes also contain other contacts, such as Hg···S [3.836(3) Å] (spodium bond/SpB) and N···S [3.795(3) Å] (chalcogen bond/ChB) in **1** (Fig. 2b); Hg···Se [3.919(4) Å] (spodium bond) and N···Se [3.838(1) Å] (chalcogen bond) in **2** (similar Fig. 2b, where Se in place of S). Nonetheless, these interactions are still significant in establishing the packing structure of both complexes. It is noteworthy that pseudohalides based on Hg(II) complexes, SpB

Table 1 Geometric features (distances in Å and angles in °) of the π⋯π interactions obtained in complexes **1** & **2**

Cg⋯Cg (ring)	Cg⋯Cg (Å)	Cg⋯I (Å)	Cg⋯J (Å)	Symmetry
Complex 1				
Cg(2)⋯Cg(2)[a]	3.569(5)	3.396(4)	3.397(4)	2 − *x*, 1 − *y*, 1 − *z*
Cg(2)⋯Cg(3)[a]	3.743(6)	3.383(4)	3.453(4)	2 − *x*, 1 − *y*, 1 − *z*
Complex 2				
Cg(2)⋯Cg(2)[a]	3.602(8)	3.409(4)	3.409(4)	2 − *x*, 1 − *y*, 1 − *z*
Cg(2)⋯Cg(3)[a]	3.722(9)	3.404(4)	3.450(5)	2 − *x*, 1 − *y*, 1 − *z*

[a] Cg(2) = centre of gravity of the ring [N(2)–C(8)–C(7)–C(6)–C(5)–C(9)], Cg(3) = centre of gravity of the ring [C(1)–C(2)–C(3)–C(4)–C(5)–C(6)] for complex **1** and Cg(2) = centre of gravity of the ring [N(2)–C(8)–C(7)–C(6)–C(5)–C(9)], Cg(3) = centre of gravity of the ring [C(1)–C(2)–C(3)–C(4)–C(5)–C(9)] for complex **2**.

concepts, are rare in the literature. However, in other classes of Hg(II) complexes, the existence of such bonding is common. Therefore, we compare the synthesized Hg⋯X (X = S/Se) SpB distances with those of other Hg(II) complexes. Mahmoudi *et al.*[19] in $[Hg(HL)(SCN)_2]$ complex explore two Hg⋯N spodium bonding nature with a distance 2.574(3) Å. Singh *et al.*[75b] showed unconventional Hg⋯Cl spodium bond in complex like $[(C_5H_3N(NH_2)_2C_{l2}Hg)]_n$ with a distance 2.9203(17) Å. Mahmoudi *et al.*[75c] further reported Hg⋯I category spodium bond in $[Hg(L^I/L^2)I]_n$ coordination polymers, with a distance of 2.6217(5)–2.6430(6) Å. Alizadeh and his research group[20] explore the existence of Hg⋯Cl type spodium bond in the $[Hg_2(HL)Cl_4]_n$ CP and the SpB distance value within the range 2.377(6)–2.378(6) Å. Sheikh *et al.*[75d] successfully showed the Hg⋯I form a spodium bond in an Hg(II) complex, $[C_{13}H_{10}N_4O_3I_2Hg]$. Such distance falls within the range of 3.407 Å. Based on CSD search, Gomila *et al.*[38] explore the Hg⋯S type spodium bonding nature for Hg(II) 1,1-dithiolate compounds with 3.35 Å. Hazra *et al.*[36] established a Hg⋯Cl spodium bond in Hg(II) complexes with distances of 2.293(3) to 3.097(3) Å. On the other hand, our synthesized Hg(II) complexes exhibit novel N⋯X (X = S/Se) ChBs. To date, no such bonding feature has been reported in the literature. We have compared these bond distances with those reported in the literature for Hg(II) complexes, where the chalcogen bonding features differ. Notably, Asaduzzaman *et al.*[75e] showed the Hg⋯Se chalcogen bond distance in $[Tm^{But}HgSePh]$ is 2.3784 Å. Kushwaha *et al.*[32] explore the O⋯S chalcogen bonding in the 1D-phenylmercury(II) CP. Here, the distances of chalcogen bonds are found to be around 2.928(5) Å. Tehrani and his dedicated research team[75f] synthesized three Hg(II) CPs containing bis(4-pyridyl) disulfide with S⋯X type chalcogen bond. Lobana *et al.*[75g] reported Hg⋯S chalcogen bond in the complex of $HgBr_2(dppeS_2)$ with a bond distance value 2.552(2)–2.678(2) Å. Therefore, the synthesized Hg(II) complexes of SpB/ChB exhibit bond distances comparable to those reported in the literature, confirming the novel bonding features.

In this context, we correlate Hirsfeld surface (HS) contacts in Hg(II) complexes (Experimental details in Section S4).[68,75] Fig. S13 and S14 shows the graphs (d_e and shape index) and 2D fingerprint plots. In **1**, the d_{norm} and shape index revealed the presence of five red spots, which signify H-bonding interactions contributing to the stability of the crystal lattice. For **1**, the principal interactions identified are H⋯H, Cl⋯H, S⋯H, H⋯C, and N⋯H, accounting for 24.3%, 18.1%, 11.1%, 10.8%, and 9.9%, of the total surface area, respectively. Similarly, for **2**, the d_{norm} and shape index reveal that the complex is also stabilized by five strong hydrogen bonding interactions, represented by red colors. The main contacts in this system include H⋯H, Cl⋯H, Se⋯H, N⋯H and Se⋯C, which cover 24.2%, 18.0%, 11.2%, 10.0% and 5% of all HS surface area. Furthermore, both Hg(II) complexes exhibit interactions with low contributions that enhance some atomic arrangement, thereby facilitating stable crystal packing. Specifically, **1** features interaction such as C⋯C, Cl⋯C, C⋯S, S⋯Hg, while **2** includes Cl⋯C, Cl⋯Hg, Se⋯Hg, and N⋯N interactions. Notably, these interactions account for less than 7% of the total interactions in **1** and 2% in **2** for all HS. Furthermore, based on the shape index iso-surface, we observe adjacent red and blue triangular patches, as highlighted by the circles and arrows. This pattern serves as an indicator, a signature of π–π stacking interactions between aromatic moieties. These are also highlighted by QTAIM and the experimental findings. A correlation between HS and 2D fingerprint plots confirms that our complexes are well stabilized, aligning with experimental results. This finding enhances the potential for selection of these newly discovered materials for targeted applications. Fig. S14a shows the HS histogram illustrating the overall percentage contributions.

6. DFT investigations

6.1. Optimized structures

We have extracted complex CIF files from X-ray diffraction analyses and, after inputting these files into Gauss View. Fig. S15 represents the optimized structure of the Hg(II) complexes. In Table S2, we have shown a correlation between experimental and DFT-computed bond distances (Å) and angles (°) for the Hg(II)-8-aq complexes. The Cartesian coordinates (vibrational frequencies) for both optimized Hg(II) complex structures have been provided in Tables S5 and S6.

6.2. FMO and DOS

The FMO (HOMO–LUMO) orbitals primarily investigates the electronic and optical characteristics of the synthesized Hg(II) complexes.[76,77] Accordingly, the donor (D) and acceptor (A) groups in the compound consider the electronic charge transfer (ECT) mechanism at the surface.[77] Additionally, the HOMO–LUMO (H–L) energy difference, commonly referred to as the band gap energy, enables conductive behaviour and various target applications.[22,46,77] Fig. 5a illustrates the HOMO and LUMO orbitals for complexes. In **1**, the HOMO orbital is predominately localized around the S–CN group. Furthermore, these electrons cross the forbidden band of 4.01 eV, with significant localization around the aromatic ring and Cl–C (carbon) groups while showing minimal localization around the carbon (C) and amine (NH_2) groups. This finding suggests that

a significant charge transfer (CT) is involved on the surface of complex materials, enhancing the conductivity of the compound. For **2**, the HOMO–LUMO orbital results are like those of **1**. However, the substation of sulfur (S) with selenium (Se) improves the chemical, reactivity, and optical properties of the Hg(II) compound, resulting in a decrease in the gap energy to 3.76 eV. The reduced HOMO–LUMO gaps obtained for **1** and **2** indicate that the electronic transitions require comparatively lower excitation energy, a feature commonly associated with semiconducting materials. The frontier orbital distribution reveals a pronounced charge-transfer pathway, where electron density flows from the quinoline donor units toward the pseudohalide acceptor groups. This charge redistribution generates partially delocalized states, which in turn can facilitate electron mobility within the extended solid-state framework. Moreover, the MEP and NBO results underline the stabilization of these charge-separated configurations through favorable donor–acceptor interactions, suggesting that the complexes possess intrinsic electronic flexibility. Collectively, these electronic attributes establish a direct link between the quantum chemical descriptors and potential device performance, thereby reinforcing the argument that these complexes are promising candidates for electronic transport in nano-electronic applications. Further, **2** is characterized by high electrical transport activity and stability. This finding indicates that **2** exhibits better conductivity than **1** and is particularly well-suited for applications in new electronic modules. The ionization potentials are 6.68 eV and 6.52 eV for **1** and **2**, respectively. The electron affinities are 2.67 eV and 2.75 eV for **1** and **2**, respectively. The above findings reveal the kinetic and chemical stability of our complexes. The density of states (DOS) illustrated in Fig. 5b further supports the conclusions of the FMO,

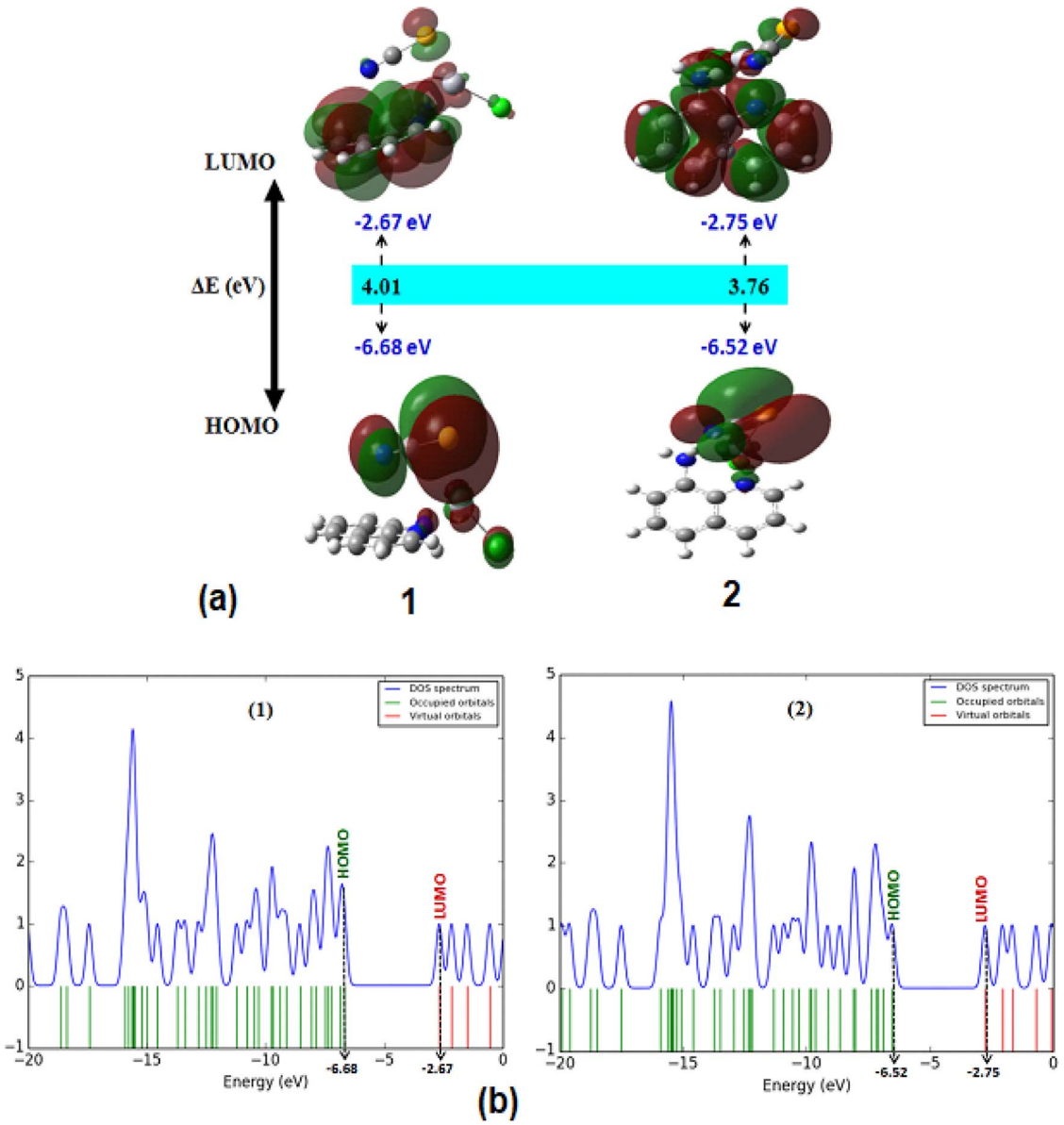

Fig. 5 (a) FMO iso-surface, (iso-value = 0.01), and (b) density of state (DOS) for Hg(II) complexes.

affirming that both complexes are strong contenders for potential new nano-electronic devices.

6.3. ELF and LOL iso-surfaces

To consider and predict the localization and delocalization of electron density of Hg(II) complexes, we employed the electron localization function (ELF) and localized orbital locator (LOL).[78,79] These computational tools elucidate the CTM (charge transfer mechanism) occurring on the surfaces of the compounds. These tools' colour scales (blue and red) range from 0 to 1 for ELF and from 0 to 0.8 for LOL.[80] An ELF value greater than 0.5 indicates the existence of bonding and nonbonding electrons, while an ELF value less than 0.5 specifies delocalized electrons. LOL, analysis is particularly effective for assessing the delocalization of electrons. Fig. 6 shows 2D-ELF and 2D-LOL plots. The 2D-ELF and 2D-LOL iso-surfaces are generated in the (*XY*) plane (see optimized Fig. S15). In **1**, a dark red colour surrounding H20, H6, and C11–C19 groups indicates the localization of high-bonding electrons in these areas. The ELF value is obtained as high as **1**. A blue colour around C8 and Hg1 signifies the presence of delocalized electrons at these sites. This observation suggests potential charge transfer on the surface of **1**, which enhances the atomic and bonding organization and the stability of the complex. For **2**, a red colour around H22 and C8–C12 confirmed the presence of excess lone pairs in these regions, while a blue colour around C6, Cl3, Hg1, and Se2 indicates the presence of delocalized electrons. These results suggest significant charge transfer on the surface of **2**, which is further supported by FMO analyses, thereby enhancing the stability of this complex. The 2D-ELF and 2D-LOL maps demonstrated significant charge transfer occurring at the surfaces of both materials, indicating the stability of the groups composing our complexes and enhancing the organization of the crystal lattice.

6.4. NLO activities

To examine the Hg(II) complexes (**1** and **2**) NLO activities, the fundamental principles of NLO are discussed in Section S5. Herein, the discussion focuses solely on the key mathematical data of the NLO, as presented in Table 2 and its accompanying textual explanation, which convey the results more straightforwardly. The core findings of the NLO analysis demonstrate that mercury complexes exhibit superior performance in terms of dipole moment, polarizability, and first hyperpolarizability, with **2** emerging as the better candidates. The compounds **1** (6.654 D) and **2** (7.042 D) have larger dipole moments in

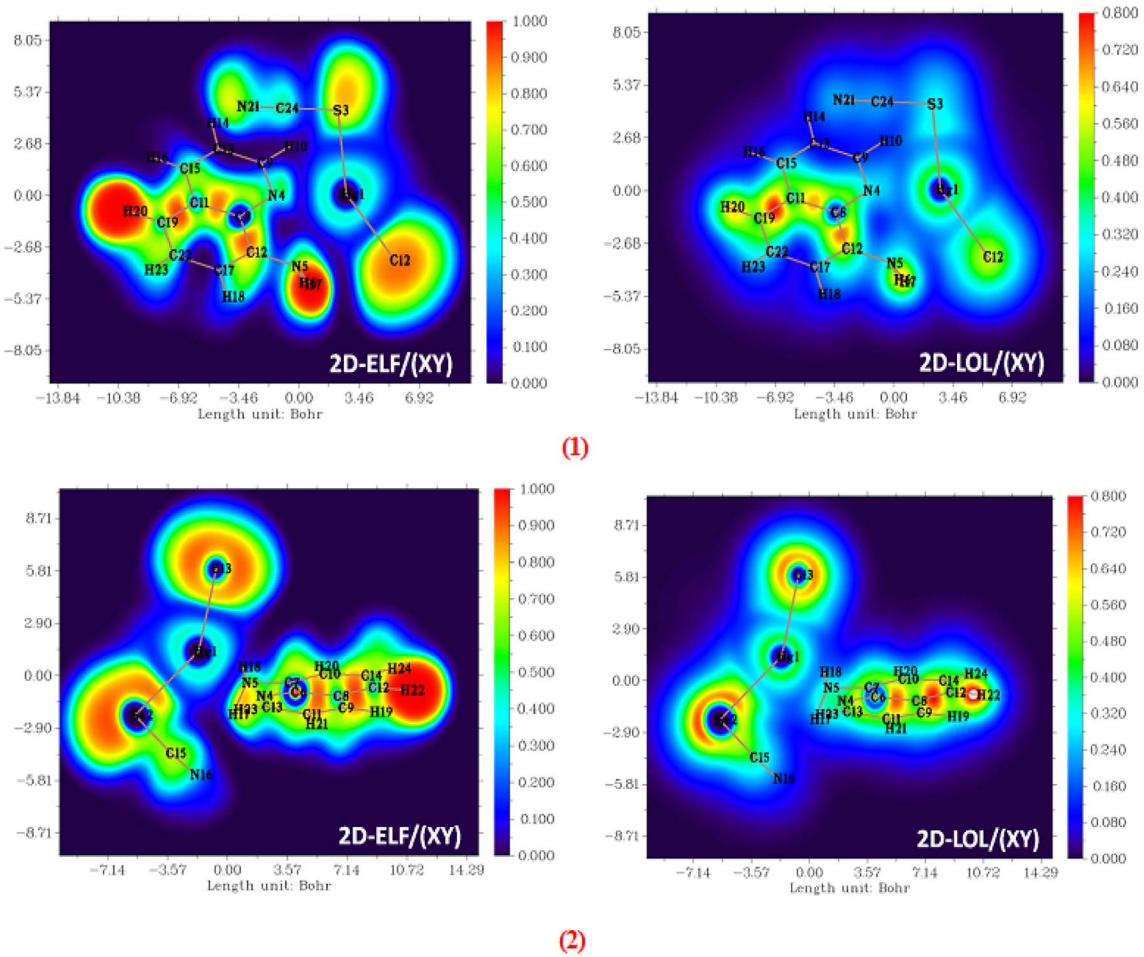

Fig. 6 2D-ELF and 2D-LOL iso-surfaces of studied Hg(II) compounds.

comparison to the reference molecule, urea. This finding explores greater charge separation and enhances intramolecular charge transfer (ICT). This higher polarity is critical for improved NLO efficiency. Similarly, the isotropic polarizabilities of **1** (26.339×10^{-24} esu) and **2** (27.800×10^{-24} esu) are more than five times greater than urea's (5.047×10^{-24} esu), indicating a substantially greater ease of electron cloud distortion in Hg(II) complexes. The lower anisotropic polarizability of **2** (10.294×10^{-24} esu) compared to **1** (12.534×10^{-24} esu) suggests a more uniform distribution of polarizability, enhancing its optical stability. In terms of first hyperpolarizability, **1** (3.395×10^{-30} esu) and **2** (4.472×10^{-30} esu) outperform urea (0.3728×10^{-30} esu) by approximately 9 and 12 times, respectively, making them highly promising for second-order NLO applications. The ratio of vector hyperpolarizability to total hyperpolarizability ($|\beta_v^{ec}|/\beta_0$) and the orientation angle (θ) between the hyperpolarizability vector and dipole moment offer key insights into molecular charge transfer pathways for Hg(II) complexes.[79] For **2**, the $|\beta_v^{ec}|/\beta_0$ ratio (0.638) and smaller θ (50.08°) compared to **1** ($|\beta_v^{ec}|/\beta_0 = 0.332$, $\theta = 70.63°$) highlight a more efficient alignment of its hyperpolarizability vector with its dipole moment. This improved alignment enhances the ICT mechanism, critical for achieving superior NLO responses. The unusual NLO properties of the compounds arise from their extended π-conjugation and increased intramolecular charge transfer (ICT), which enhances electronic polarizability and nonlinear responses. These results position **1** and **2**, especially **2**, as up-and-coming candidates for advanced photonic and optoelectronic applications, such as second-harmonic generation (SHG), frequency doubling, and electro-optic modulation. The compounds NLO superior properties pave the way for next-generation materials with enhanced performance in integrated optical devices. Future work should focus on experimental validation and exploration of higher-order NLO properties to fully realize their potential in fundamental research and technological applications.

Table 2 NLO calculated parameters for Hg(II) complexes

Complexes	1	2
Electric dipole moment		
μ_X	−5.931	−5.418
μ_Y	−2.929	−2.443
μ_Z	0.718	−3.775
μ_{tot} (Debye)	6.654	7.042
Dipole polarizability, alpha (α, $\times 10^{-24}$ esu)		
α_{iso}	26.339	27.800
α_{aniso}	12.534	10.294
α_{XX}	32.490	26.523
α_{YX}	−2.202	−0.838
α_{YY}	24.711	26.219
α_{ZX}	2.229	5.267
α_{ZY}	3.475	−0.845
α_{ZZ}	21.817	30.660
First dipole hyperpolarizability, beta (β, $\times 10^{-30}$esu)		
β_{XXX}	−1.589	−1.781
β_{XXY}	2.238	−0.098
β_{YXY}	−0.165	−0.248
β_{YYY}	−0.959	−1.430
β_{XXZ}	−0.624	1.996
β_{YXZ}	0.163	−0.461
β_{YYZ}	1.094	−0.409
β_{ZXZ}	−0.250	−0.296
β_{ZYZ}	−0.085	−1.295
β_{ZZZ}	1.189	−4.729
β_0	3.395	4.472
$\lvert\beta^{vect}\rvert\left(\beta^{vec} = \sum_i \frac{\beta_i \mu_i}{\mu} \quad [i = x, y, z]\right)$	1.128	2.855
$\frac{\lvert\beta^{vect}\rvert}{\beta_0}$	0.332	0.638
$\Theta(^\circ), \quad \left(\cos(\theta) = \frac{\beta^{vec}}{\beta_0}\right)$	70.63	50.08

7. X-ray crystallography and DFT

In complexes, Hg(II) is coordinated to 8-aq in a bidentate *N*,*N* chelating fashion, with the coordination sphere completed by chloride and either thiocyanate or selenocyanate as anionic ligands. In the solid state (Fig. 7a and b), these compounds exhibit an intricate network of noncovalent interactions, including Hg···Cl, Hg···S, and Hg···Se contacts, which have been analysed in detail. Within the trimeric assemblies depicted in Fig. 7a and b, the N-atom of the thiocyanate in **1** or selenocyanate in **2** interacts with the Hg atom at distances of 3.602 Å in **1** and 3.577 Å in **2**, both shorter than the sum of Batsanov's van der Waals radii (3.65 Å). Additionally, the Hg atom is proximate to the S or Se atom of an adjacent molecule (3.836 and 3.919 Å, respectively), also shorter than the corresponding ΣR_{vdW} values (3.88 Å for Hg + S and 3.98 Å for Hg + Se). Furthermore, an additional Hg···Cl contact is established at 3.836 Å in **1** and 3.860 Å in **2**, also shorter than the ΣR_{vdW} (3.88 Å for Hg + Cl). All these interactions are recognized as spodium bonds (SpBs), a term that describes noncovalent interactions where a group of 12 elements acts as an electron acceptor (A). The accompanying DFT study provides a detailed energetic analysis of these contacts and characterizes them using advanced computational tools, including QTAIM, NCI plot, and MEP surface analyses.

7.1. Non-covalent interactions

As the initial step in the theoretical investigation, Molecular Electrostatic Potential (MEP) surface analysis was conducted for both complexes to identify the most nucleophilic (Nu) and electrophilic (*E*) regions of the molecules (Fig. 8a and b). This analysis provides a detailed visual representation of charge distribution across the molecular surfaces, highlighting areas susceptible to electron donation or acceptance. The finding reveals that in both Hg(II) complexes, the maximum MEP is located at the H-atoms of the amino group (+57.1 and +56.5 kcal mol^{-1} for **1** and **2**, respectively), while the minimum is at the N-atom of the pseudohalide (−45.2 kcal mol^{-1} for **1** and −43.3 kcal mol^{-1} for **2**). Additionally, the chloride ligands exhibit significantly negative MEP values (−42.7 kcal mol^{-1} in both complexes). The −42.7 number is in located in the very top of Fig. 6b. These large MEP values at the NH_2 group and the anionic co-ligands (SCN^-/$SeCN^-$) align with the observed

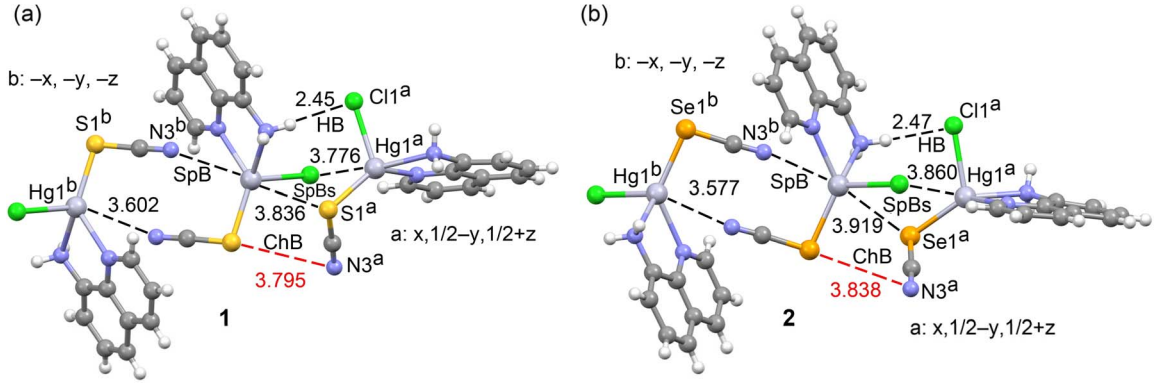

Fig. 7 Partial views of the solid-state X-ray structures of **1** (a) and **2** (b) showing trimeric assemblies (distances in Å).

formation of strong NH···Cl and NH···N interactions in the solid state, though such interactions are not the focus of this study. The MEP values over the π-systems of the aromatic rings range from +16.3 to +19.5 kcal mol^{-1}, reflecting the π-acidity of the rings, which arises due to the coordination of the 8-aq ligand to Hg(II). The MEP at the Hg atom is also positive (+17.6 kcal mol^{-1} in **1** and +15.7 kcal mol^{-1} in **2**), supporting the formation of spodium bonds (SpBs). Notably, the MEP around the chalcogen atoms (S or Se) is significantly anisotropic, displaying a negative belt with a minimum of −25.7 kcal mol^{-1} in **1** and −24.9 kcal mol^{-1} in **2**. In contrast, the chalcogen atoms also exhibit a σ-hole directly opposite the C–Ch bond, with values of +1.3 kcal mol^{-1} in **1** and +8.8 kcal mol^{-1} in **2**, which may correlate with the formation of weak chalcogen bonds (reflected by the red dashed lines in Fig. 8a and b). Interestingly, the N-atom of the pseudohalide is positioned opposite the C–Ch bond at distances longer than the sum of van der Waals radii (ΣR_{vdW}: 3.40 Å for N + S and 3.50 Å for N + Se). These special contacts, characterized by weak noncovalent interactions, are further elaborated in subsequent sections.

7.2. QTAIM/NCI plot

We analysed two dimers for each compound, extracted from the trimeric assemblies shown in Fig. 7a and b. Dimers in which two symmetrically equivalent Hg···N contacts are established are denoted as dimers "A". Their combined QTAIM/NCI plot analyses are presented in Fig. 9a and b. The analysis's primary findings are that the spodium bonds (SpBs) are characterized by bond critical points (BCPs, represented as small red spheres) and bond paths (orange lines) linking the Hg atom to the N atoms of the pseudohalides, confirming the existence of these interactions. Additionally, the SpBs are associated with green reduced density gradient (RDG) iso-surfaces that align with the locations of the BCPs. The QTAIM/NCI plot analysis also shows that the N-atom of the pseudohalide interacts with a C-atom of the aromatic system *via* a BCP and bond path, indicating the formation of additional LP···π interactions that further stabilize the self-assembled dimer. Notably, an intriguing feature of these centrosymmetric dimers is the connection of CN (cyano groups) in the SCN^-/$SeCN^-$ (pseudohalides) through a BCP and bond path, indicating an antiparallel π···π interaction. The dimers' interaction energies (IEs) are similar, at −21.2 kcal mol^{-1} for **1** and −20.4 kcal mol^{-1} for **2**.

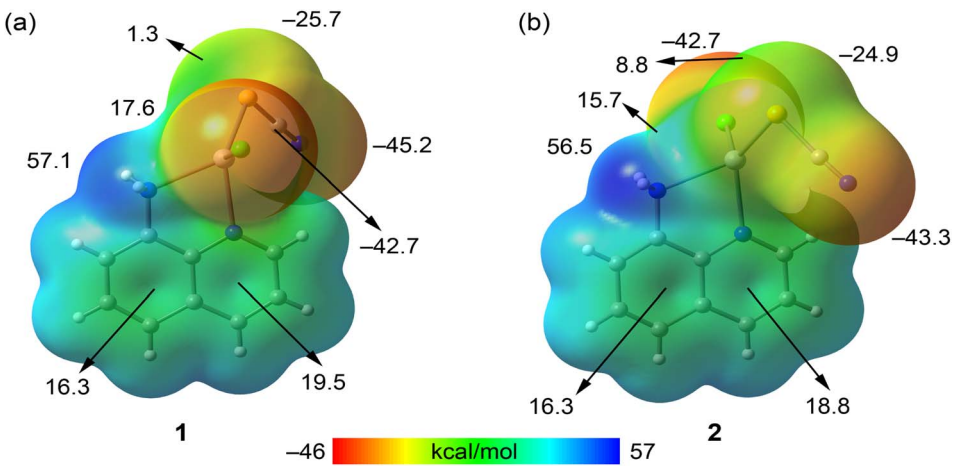

Fig. 8 MEP surfaces of **1** (a) and **2** (b) (energies at selected points in kcal mol^{-1}).

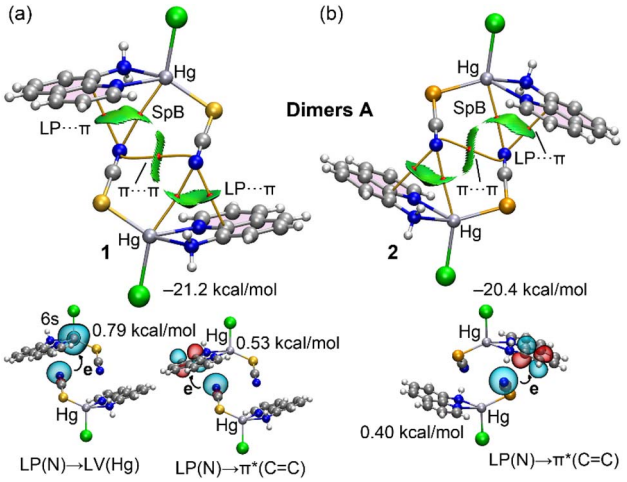

Fig. 9 QTAIM (BCPs in red and bond paths as orange lines) and NCI Plot (RDG = 0.5 au) analyses of centrosymmetric dimers A of **1** (a) and **2** (b). Only intermolecular interactions are represented. The NBOs involved in the LP → π* and LP → 6s are indicated along with the second order perturbation energies (the symmetry operation to generate the dimer is −*x*, −*y*, −*z*).

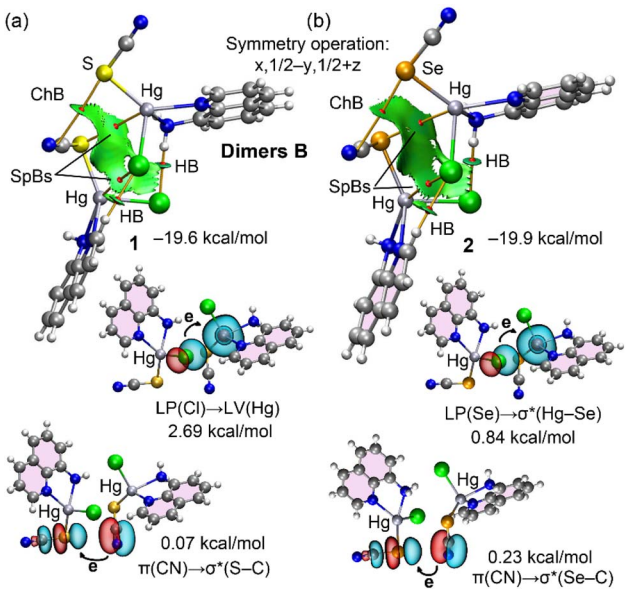

Fig. 10 QTAIM (BCPs in red and bond paths as orange lines) and NCI Plot (RDG = 0.5 au) analyses of centrosymmetric dimers B of **1** (a) and **2** (b). Only intermolecular interactions are represented. The NBOs involved in the LP → π* and LP → 6s are indicated along with the second order perturbation energies.

7.3. NBO analysis

We further conducted an NBO analysis to survey the role of orbital donor–acceptor effects in these interactions (Fig. 10a and b, bottom). Given the relatively long distances in these contacts, significant orbital overlap is not expected, and the observed effects are small. In Hg(II) compounds, N-atom electron donation *via* lone pair (LP) of the pseudohalides (SCN^-/$SeCN^-$) to the π* antibonding orbital of the aromatic ring was identified, confirming the LP···π interaction. However, the associated orbital stabilization energies are minor (<1 kcal mol^{-1}). In **1**, where the Hg···N distance is shorter, additional electron donation from the LP of the pseudohalide N-atom to an empty 6s atomic orbital of Hg was observed, with an associated stabilization energy of 0.53 kcal mol^{-1}. This finding further supports the spodium bond nature of this contact. The same analysis for centrosymmetric dimers **B** was performed and is represented in Fig. 10a and b. A more complex distribution of BCPs and bond paths is observed in these dimers. Expressly, the QTAIM analysis supports proof of combined Hg···Ch and Hg···Cl spodium bonds (SpBs), featured by corresponding BCPs, bond paths, and green reduced density gradient (RDG) iso-surfaces, which confirm their attractive nature. Moreover, the NH···Cl and CH···Cl H-bonds are formed, providing additional connections between the two monomers. Notably, the combined QTAIM/NCI plot evaluation indicates the presence of chalcogen (Ch)···N chalcogen bonds in each of the two compounds. These interactions are also featured by BCPs, bond paths, and green RDG iso-surfaces, even though the distances involved are approximately 0.4 Å longer than the sum of the van der Waals radii (ΣR_{vdW}). The dimerization energies for these dimers are similar those observed for centrosymmetric dimers **A** (~20 kcal mol^{-1}) in both cases. Based on the NBO analysis, shown in the lower part of Fig. 10a and b, further supports the existence of the Ch···N chalcogen bonds, as it reveals electron donation from the π-orbital of the CN group to the antibonding σ*(Ch–C) orbital, which is characteristic of σ-hole interactions. The analysis further reveals that the electron donation from Cl or Se to the Hg 6s or antibonding Hg–Se orbital in **1** and **2** confirms the presence of spodium bonds.

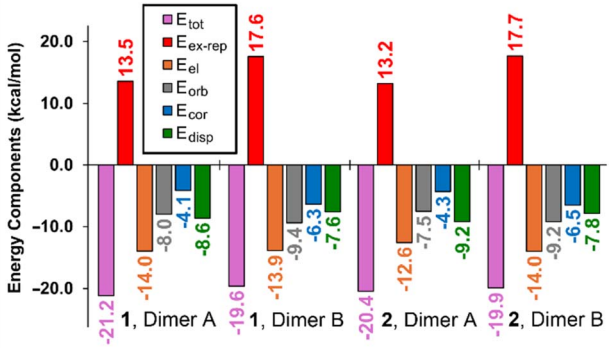

Fig. 11 EDA of centrosymmetric dimers A and B in **1** and **2** (energies in kcal mol^{-1}).

7.4. Energy decomposition analysis (EDA)

We also performed EDA to investigate the relative contributions of electrostatic (E_{el}), orbital (E_{orb}), correlation (E_{cor}), and dispersion (E_{disp}) interactions in the formation of the dimers. The results in Fig. 11 indicate that the electrostatic term (E_{el}) is the most significant attractive component in all cases. In centrosymmetric dimers **A**, the second-largest contribution comes from dispersion (E_{disp}). Besides, the orbital interaction

term (E_{orb}) dominates for centrosymmetric dimers **B**, which is likely due to the interactions in the two types of dimers. In centrosymmetric dimers **A**, the formation of LP$\cdots\pi$ interactions, which are strongly influenced by dispersion forces, enhances the contribution of the dispersion term. Furthermore, for centrosymmetric dimers **B**, H-bonds significantly increase the contribution of the orbital term. The term' orbital interactions' stabilizes H-bonds after accounting for the dominant electrostatic contributions. These findings highlight the varying interactions between the two types of dimers.

8. Biological implications

8.1. Antimicrobial activity

Table 3 explores the antibacterial and antifungal activities of Hg(II) salts and their associated compounds. The antimicrobial activity, measured by the inhibition zone diameter, is illustrated in Fig. 12. The inhibition zone diameters against Gram-positive bacteria (*S. aureus* and *B. subtilis*) are as follows: for *Staphylococcus aureus*, 24 $\pm$ 0.1, 22 $\pm$ 0.2, 10 $\pm$ 0.1, and 8 $\pm$ 0.3 mm for **1**, **2**, $HgCl_2$, and 8-aq, respectively, and *Bacillus subtilis*, 18 $\pm$ 0.3, 25 $\pm$ 0.4, 11 $\pm$ 0.1, and 10 $\pm$ 0.2 mm for **1**, **2**, $HgCl_2$, and 8-aq, respectively. The finding reveals that **1** and **2** exhibit moderates to high activity against the selected Gram-positive microbes, with **2** showing higher activity against *Bacillus subtilis*. At the same time, both **1** and **2** demonstrate similar activity against *Staphylococcus aureus*. However, against *E. coli*, only complexes **1** and **2** show activity, with inhibition zone diameters of 15 $\pm$ 0.2 and 16 $\pm$ 0.1 mm, respectively. The antifungal efficacy against *Candida albicans* and *Aspergillus fumigatus* is shown: 25 $\pm$ 0.1, 17 $\pm$ 0.2, 15 $\pm$ 0.1, and 13 $\pm$ 0.3 mm for **1**, **2**, $HgCl_2$, and 8-aq, respectively, against *Candida albicans*, and 13 $\pm$ 0.1, 15 $\pm$ 0.4, 10 $\pm$ 0.1, and 10 $\pm$ 0.3 mm for **1**, **2**, $HgCl_2$, and 8-aq, respectively, against *Aspergillus fumigatus*. These results indicate that **1** exhibit moderate to high antifungal activity against *Candida albicans*, while the other compounds show low to medium activity. However, all compounds display very low activity against *Aspergillus fumigatus*. None of the synthesized Hg(II) compounds demonstrates activity more significant than the selected standard drug, though the complexes show relatively higher activity against the tested microorganisms. Hg(II) complexes demonstrating significant bacterial inhibition were evaluated for their minimum inhibitory concentration (MIC). MIC values were determined for the selected bacterial strains using the resazurin reduction assay in 96-well microtiter plates. Only the compounds with potent antibacterial activity against multiple bacterial strains were chosen for MIC analysis (Table 4). The results were then compared to those of the standard drug.

8.2. Structure–activity relationship

The antibacterial and fungal efficacy was correlated with structure–activity relationship (SAR) based on the complexes synthetic Scheme 1. The 8-aq and $HgCl_2$ show little to no activity against the microbes chosen, but their Hg(II) complexes, being more active upon bidentate 8-aq ligand chelation, are concerned with Tweedy's chelation theory.[49,68] Chelation lowers the polarity of the Hg(II) atom by partially sharing its positive charge with 8-aq. The complex's e-delocalization through ligands enhances lipophilicity, aiding penetration through microbial membrane lipid layers. Table 3 shows that metal complexes exhibit low antimicrobial activity. Notably, reduced inhibitory performance may stem from L–L (low-lipophilicity), which hinders metal complexes' ability to penetrate L–M (lipid-membranes). Again, Hg(II) metal ions in complexes with spacers SCN^-/$SeCN^-$ were more effective in destabilizing membranes than the free 8-aq, disrupting cell integrity and eradicating the microorganism. **1** and **2** showed moderate to high IZ (inhibition zones), indicating bactericidal activity against Gram-positive bacteria (*Staphylococcus aureus* and *Bacillus subtilis*). Similarly, the finding displayed moderate to strong IZD (inhibition zone diameters) and demonstrated antifungal activity against *Candida albicans* and *Aspergillus fumigatus*.

8.3. Cytotoxicity analysis

The *in vitro* cytotoxicity of Hg(II) compounds was assessed against DLA cells (Dalton's Lymphoma Ascites) using the TBA (Trypan blue assay) (Fig. 13a) and against HepG2 (human hepatocellular carcinoma) and non-carcinogenic H9c2 (Embryonic BD1X Rat Heart Tissue) cell lines (Fig. 13b). Tables 5 and 6 shows the percentage of cell viability for the tested compounds. Experiments on H9c2 cell lines using the MTT

Table 3 Antimicrobial findings of the synthesised compounds

	Bacteria strains and inhibition zone diameter (mm)					
	Gram-positive bacteria		Gram-negative bacteria		Yeast and fungi	
Sample code	*S. aureus* (ATCC 5923)	*B. subtilis* (ATCC 6635)	*E. coli* (ATCC 25922)	*S. typhimurium* (ATCC 14028)	*C. albicans* (ATCC 10231)	*A. fumigatus*
1	24 $\pm$ 0.1	18 $\pm$ 0.3	15 $\pm$ 0.2	—	25 $\pm$ 0.1	13 $\pm$ 0.1
2	22 $\pm$ 0.2	25 $\pm$ 0.4	16 $\pm$ 0.1	11 $\pm$ 0.3	17 $\pm$ 0.2	15 $\pm$ 0.4
$HgCl_2$	10 $\pm$ 0.1	11 $\pm$ 0.1	—	8 $\pm$ 0.1	15 $\pm$ 0.1	10 $\pm$ 0.1
8-aq	8 $\pm$ 0.3	10 $\pm$ 0.2	—	—	13 $\pm$ 0.3	10 $\pm$ 0.3
Control	35 $\pm$ 0.2	35 $\pm$ 0.3	36 $\pm$ 0.2	38 $\pm$ 0.3	35 $\pm$ 0.2	37 $\pm$ 0.1
DMSO	0	0	0	0	0	0

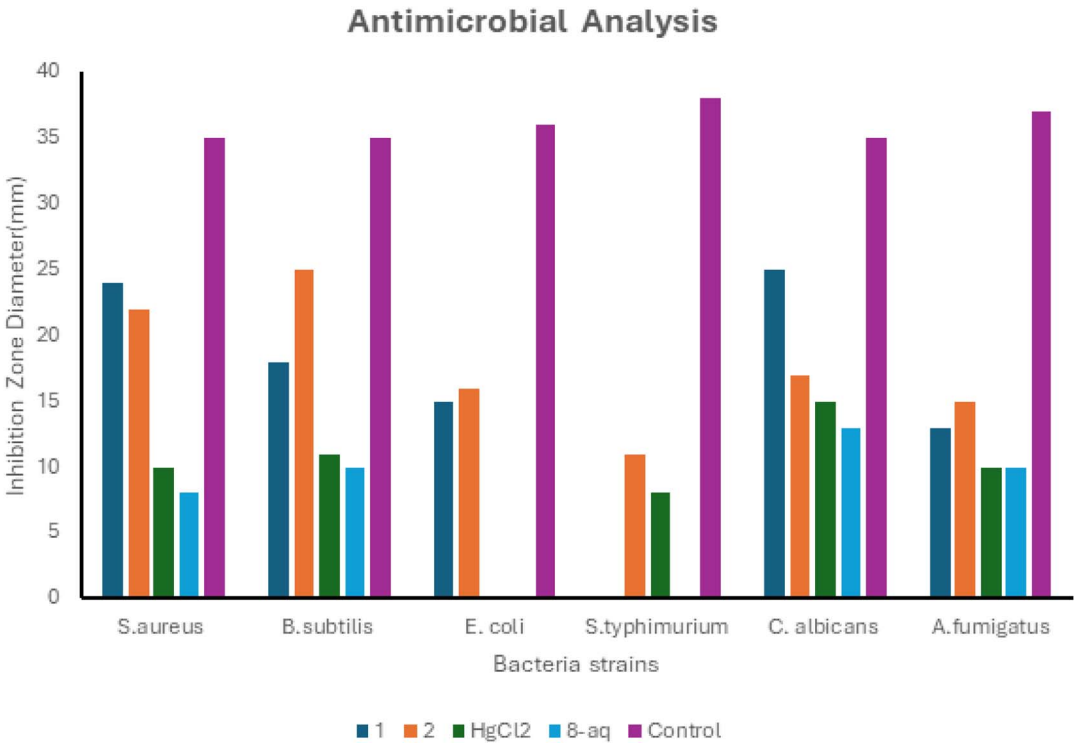

Fig. 12 Hg(II) complexes antimicrobial efficacy against different strains.

Table 4 Selected compounds MIC values

	MIC values (μg mL^{-1})	
	Gram positive	
Compounds	*S. aureus*	*B. subtilis*
1	72.1	62.7
2	42.5	50.4
Control	>7	>7
DMSO	—	—

assay reflect a concentration-dependent decrease in cell viability at 1, 5, 10, and 25 μg mL^{-1} of the Hg(II) compounds. **1** exhibited low cytotoxicity, with values of 29.44 ± 1.0, 24.42 ± 1.4, 13.24 ± 1.4, and 1.52 ± 1.4 μg mL^{-1} for HepG2 cells, and 40.91 ± 1.5, 29.12 ± 1.0, 14.52 ± 1.6, and 6.49 ± 2.0 μg mL^{-1} for H9c2 cells. Other compounds showed limited potential to inhibit malignant cell growth at higher concentrations, as reflected the results in the MTT assay. Based on the Trypan blue exclusion assay, all compounds demonstrated weak cytotoxic effects on DLA cell lines. Overall, the tested concentrations (200, 150, 100, 50, 25, and 12.5 μg mL^{-1}) exhibited relatively low cytotoxicity compared to the control. At 200 μg mL^{-1}, the percentage of cell viability was 11.50 ± 1.4% for **1**, 10.59 ± 2.6% for **2**, 7.67 ± 1% for $HgCl_2$, and 7.67 ± 1% for 8-aq, which was statistically significant compared to the control. At lower concentrations, **1** showed cell viability percentages of 24.1 ± 0.7%, 35.68 ± 1.3%, 51.38 ± 1.7%, 82.20 ± 2.1%, and 95.36 ± 1.6% for 150, 100, 50, 25, and 12.5 μg mL^{-1}, respectively. For **2**, the corresponding

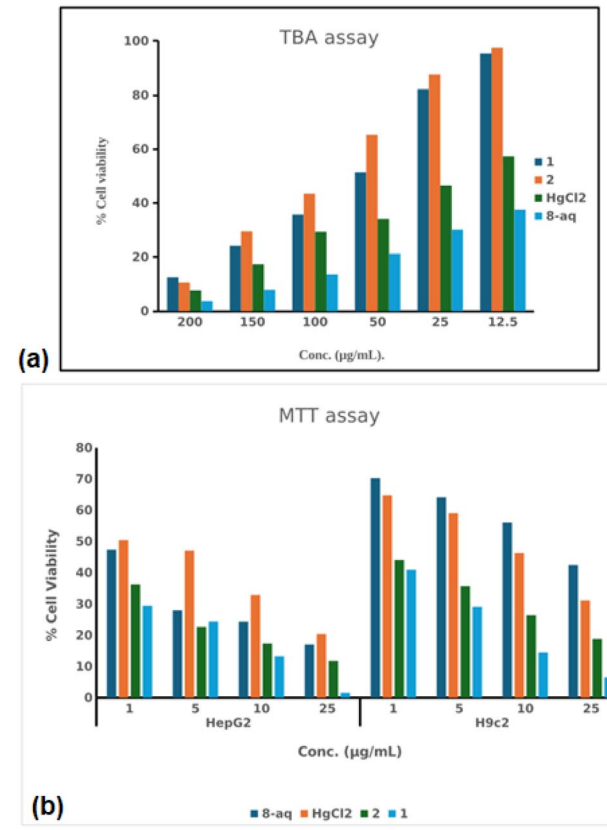

Fig. 13 (a and b) Percentage (%) cell viability by TBA and MTT assay.

Table 5 Percentage (%) cell viability by MTT assay

Compounds (μg mL^{-1})	HepG2				H9c2			
	1	5	10	25	1	5	10	25
8-aq	47.34 ± 1.2	28.01 ± 1.1	24.36 ± 2.0	17.04 ± 1.0	70.27 ± 1.1	64.17 ± 2.1	56.07 ± 2.1	42.41 ± 1.3
$HgCl_2$	50.42 ± 1.3	47.07 ± 1.4	32.93 ± 1.1	20.43 ± 0.4	64.80 ± 1.2	59.07 ± 1.0	46.27 ± 1.2	31.18 ± 1.1
2	36.31 ± 1.4	22.69 ± 1.3	17.37 ± 1.2	11.78 ± 1.2	44.04 ± 1.4	35.76 ± 1.3	26.45 ± 1.0	18.87 ± 1.4
1	29.44 ± 1.0	24.42 ± 1.4	13.24 ± 1.4	1.52 ± 1.4	40.91 ± 1.5	29.12 ± 1.0	14.52 ± 1.6	6.49 ± 2.0

Table 6 Percentage (%) cell viability synthesised compounds by Trypan Blue assay

Compounds (μg mL^{-1})	% Cell viability			
	1	**2**	$HgCl_2$	8-aq
200	11.50 ± 1.4	10.59 ± 2.6	7.67 ± 1	3.7 ± 0
150	24.1 ± 0.7	29.5 ± 1.4	17.41 ± 1.2	7.88 ± 1.5
100	35.68 ± 1.3	43.47 ± 1.1	29.36 ± 1.4	13.6 ± 1.2
50	51.38 ± 1.7	65.34 ± 0.4	34.1 ± 0.5	21.2 ± 1.6
25	82.20 ± 2.1	87.59 ± 1.2	46.48 ± 1.3	30.1 ± 1.1
12.5	95.36 ± 1.6	97.51 ± 1.5	57.34 ± 1.6	37.5 ± 1.4

percentages were 29.5 ± 1.4%, 43.47 ± 1.1%, 65.34 ± 0.4%, 87.59 ± 1.2%, and 97.51 ± 1.5%, respectively.

8.4. Cytotoxicity: a logistic reason

The cytotoxicity findings indicate that the isostructural features of the two Hg(II) complexes decrease cell viability as the concentration of the compound increases. Generally, higher concentrations can damage cell membranes, allowing trypan blue to stain dead cells. Low concentrations are less toxic, suggesting they may be safer for therapeutic use with minimal impact on healthy cells. Increased toxicity at specific concentrations is due to interactions with protein biomolecules. Functional groups with lone electron pairs and pseudohalides (SCN^-/$SeCN^-$) can play a crucial role in hydrogen bonding with DNA, affecting the overall cytotoxic efficacy.[81] Moreover, simple structural modifications based on the linker anions SCN^- and $SeCN^-$ to the metal complexes can influence their DNA-binding capabilities or their ability to form inter-strand crosslinks in double-stranded DNA, ultimately affecting their cytotoxicity. These factors account for the cytotoxicity differences found between the two Hg(II) complexes.

9. Conclusion

We synthesized and X-ray characterized two isostructural Hg(II) complexes using the 8-aq and pseudohalides SCN^- (**1**) and $SeCN^-$ (**2**). The complexes crystallized in the monoclinic space group $P2_1/c$, featuring a tetra-coordinated Hg(II) centre. The crystal networks exhibit both strong and weak hydrogen bonds, as well as π···π interactions, as supported by Hirshfeld surface and 2D fingerprint plot analysis. In **1 and2**, the Hirshfeld surface reveals strong H···H interactions, with percentages of 24.3% and 24.2%, respectively. Also, Cl···H (18.1%) and Se···H (11.2%) interactions affected the complex's crystal assembly. FMO studies suggest that Hg(II) complexes are reactive and promising conducting behaviour, based on the HOMO–LUMO energy band gap (4.01 eV for **1** and 3.76 eV for **2**). The NLO parameters, hyperpolarizability (β_0) values of 3.395×10^{-30} for **1** and 4.472×10^{-30} esu for **2**, indicate that the second complex is more suitable than the first for use in optoelectronic applications. NLO ensures that complex **2** is utilized in optoelectronic applications. The complex's X-ray structure reveals the existence of noncovalent interactions (NCI), spodium (SpB), and chalcogen bonds (ChB) in the crystal assembly, supported by QTAIM, NCI-RDG plots, NBO, and MEP surface analyses. EDA explores the role of electrostatics, highlighting dispersions in complex dimers with LP···π interactions and orbital effects in hydrogen-bonded dimers. The antimicrobial activities were tested against Gram-positive bacteria (*S. aureus* and *B. subtilis*), Gram-negative bacteria (*E. coli* and *S. typhimurium*), the fungus *A. fumigatus*, and the yeast *C. albicans*. The findings are rationalized based on MIC and the structure–activity relationship. Notably, the complexes show moderate to high activity against Gram-positive bacteria, with **2** being more effective against *B. subtilis*. The research elucidates the dose-dependent cytotoxicity of Hg(II) complexes on DLA, HepG2, and H9c2 cancer cell lines, indicating that the complexes are less toxic to H9c2 cells. It is noteworthy that the author group explored pseudohalide-based Hg(II) 8-aq complexes for the first time, combining spodium and chalcogen bonding concepts with biological efficacy. The insights presented in this article will greatly inspire and motivate future researchers in the fields of crystal engineering, DFT, and biological studies.

Author contributions

Dr Dhrubajyoti Majumdar was the project's author and conceived the entire research idea; performed data curation, conceptualization, methodology, research investigation, and formal analysis; contributed reagents, materials, and software visualization; wrote the review, prepared the initial draft, and edited the manuscript. Prof. Dr Antonio Frontera and Dr Sergi Burguera performed DFT experiments. Dr Jessica Elizabeth Philip performed formal analysis, biological study, and software visualization. Dr Bouzid Gassoumi and Dr Sahbi Ayachi performed DFT experiments. Dr Sourav Roy was involved in X-ray crystallographic work. All authors reviewed, read, and approved the final version of the manuscript before its submission.

Conflicts of interest

The authors declare that no conflicts of interest are related to the publication.

Data availability

The communicated article is a full-length research article; therefore, the new research data generations are relevant and if required, submit to the corresponding author upon reasonable request.

CCDC 2440026 and 2440027 contain the supplementary crystallographic data for this paper.[82a,b]

Supplementary information (SI) is available. See DOI: https://doi.org/10.1039/d5ra09546h.

Acknowledgements

The authors thank the Central Laboratory of Tamralipta Mahavidyalaya and the Department of Chemistry, Tamluk-721636, Purba Medinipur, WB, India. We received advanced analytical data files from STIC, Cochin, for SEM-EDX, SAIF, IIT Madras for Raman spectra, and IIT Jammu, India, for HRMS and XPS. We also acknowledge Panjab University, Chandigarh-160014, India, for support with FTIR spectral analysis. We thank all these research Institutions. The authors acknowledge Amala Cancer Centre, Thrissur, for conducting the cytotoxicity studies.

References

1 F. Blau, Die Destillation pyridinmonocarbonsaurer Salze, *Ber. Dtsch. Chem. Ges.*, 1888, **21**, 1077–1078.
2 M. K. Paria, J. Dinda, T.-H. Lu, A. R. Paital and C. Sinha, Zn(II), Cd(II) and Hg(II) complexes of 8-aminoquinoline: Structure, spectra and photoluminescence property, *Polyhedron*, 2007, **26**, 4131–4140.
3 *Comprehensive Coordination Chemistry*, ed. G. Wilkinson, R. D. Gillard, and J. McCleverty, Pergamon Press, Oxford, 1987, vol. 1–7.
4 M. Cais, *Progress in Coordination Chemistry*, American Elsevier, New York, 1968.
5 D. H. Bush, The complete coordination chemistry - one practioner's perspective, *Chem. Rev.*, 1993, **93**, 847–860.
6 M. Mirzaei, H. Eshtiagh-Hosseini, Z. Bolouri, Z. Rahmati, A. Esmaeilzadeh, A. Hassanpoor, A. Bauza, P. Ballester, M. Barceló-Oliver, J. T. Mague, B. Notash and A. Frontera, Rationalization of Noncovalent Interactions within Six New M^{II}/8-Aminoquinoline Supramolecular Complexes (M^{II} = Mn, Cu, and Cd): A Combined Experimental and Theoretical DFT Study, *Cryst. Growth Des.*, 2015, **15**, 1351–1361.
7 Y. Kim, S.-J. Kim, S. H. Choi, J. H. Han, S. H. Nam, J. H. Lee, H. J. Kim, C. Kim, D. W. Kim and H. G. Jang, Crystal structures and catalytic activities of Zn(II) compounds containing 1,3-bis(4-pyridyl) propane, *Inorg. Chim. Acta*, 2006, **359**, 2534–2542.
8 R. Kumar, A. Thakur, D. Chandra, A. K. Dhiman, P. K. Verma and U. Sharma, Quinoline-based metal complexes: Synthesis and applications, *Coord. Chem. Rev.*, 2024, **499**, 215453.
9 M. K. O'Neill, A. F. Trappey, P. Battle, C. L. Boswell and D. N. Blauch, Electrochemistry of ruthenium(II) complexes of 8-aminoquinoline, *Dalton Trans.*, 2009, 3391–3394.
10 B. L. Tekwami and L. A. Walker, 8-Aminoquinolines: future role as antiprotozoal drugs, *Curr. Opin. Infect. Dis.*, 2006, **19**, 623–631.
11 J. M. Fritsch, K. A. Thoreson and K. McNeill, Synthesis and structures of acyclic monoanionic tetradentate aza β-diketiminate complexes of magnesium, zinc, and cadmium, *Dalton Trans.*, 2006, 4814–4820.
12 B. Macias, I. Garcia, M. V. Villa, J. Borras, A. Casiineiras and F. Sanz, Synthesis and Structural Characterization of Zinc Complexes with Sulfonamides containing 8-Aminoquinoleine, *Z. Anorg. Allg. Chem.*, 2003, **629**, 255–260.
13 D. J. Harding, D. Sertphon and P. Harding, (8-Aminoquinoline-μ-2 N,N) bis(1,1,1,-5,5,5-hexafluoropentane-2,4-dionatoj2 O,O0) cobalt(II), *Acta Crystallogr., Sect. E: Struct. Rep. Online*, 2012, **68**, m450.
14 H. Xu and C. Guo, catena-Poly[(8-aminoquinoline-μ-2 N,N)-cadmium]-di-l-thiocyanato-μ2-N:S;-μ2-S:N-[(8-aminoquinoline-μ2-N,N)-cadmium]-di-l-chlorido, *Acta Crystallogr., Sect. E: Struct. Rep. Online*, 2012, **68**, m3.
15 M. Mirzaei, H. Eshtiagh-Hosseini, M. M. Abadeh, M. Chahkandi, A. Frontera and A. Hassanpoor, Influence of accompanying anions on supramolecular assembly and coordination geometry in Hg(II) complexes with 8-aminoquinoline: experimental and theoretical studies, *CrystEngComm*, 2013, **15**, 1404–1413.
16 H. Wang, P. Wang, C. Huang, L. Chang, J. Wu, H. Hou and Y. Fan, Construction of a series of mercury(II) complexes based on a bis-pyridyl-bis-amide ligand: Effect of counter anions, interactions on the supermolecular structures, *Inorg. Chim. Acta*, 2011, **378**, 326–323.
17 E. López-Torres and M. A. Mendiola, Mercury complexes with the ligand benzaldehyde-N(4), N(4)-dimethylthiosemicarbazone, *Inorg. Chim. Acta*, 2010, **363**, 1275–1283.
18 B. Notash, N. Safari and H. R. Khavasi, Anion-Directed Self-Assembly in Coordination Networks: Architectural Control *via* Cooperative Noncovalent Interactions, *Inorg. Chem.*, 2010, **49**, 11415–11420.
19 G. Mahmoudi, E. Zangrando, B. Miroslaw, A. V. Gurbanov, M. G. Babashkina, A. Frontera and D. A. Safin, Spodium bonding and other non-covalent interactions assisted supramolecular aggregation in a new mercury(II) complex of a nicotinohydrazide derivative, *Inorg. Chim. Acta*, 2021, **519**, 120279.
20 V. Alizadeh, G. Mahmoudi, M. A. Vinokurova, K. M. Pokazeev, K. A. Alekseeva, B. Miroslaw, A. A. Khandar, A. Frontera and D. A. Safin, Spodium bonds and metal–halogen···halogen–metal interactions in propagation of monomeric units to dimeric or polymeric architectures, *J. Mol. Struct.*, 2022, **1252**, 132144.

21 R. M. Gomila, E. R. T. Tiekink and A. Frontera, A Computational Chemistry Investigation of the Influence of Steric Bulk of Dithiocarbamato-Bound Organic Substituents upon Spodium Bonding in Three Homoleptic Mercury(II) Bis(N,N-dialkyldithiocarbamato) Compounds for Alkyl = Ethyl, Isobutyl, and Cyclohexyl, *Inorganics*, 2023, **11**, 468.

22 D. J. Majumdar, A. Dey, S. Roy, D. Sutradhar and S. Hazra, Embellished photosensitive Schottky barrier diode functionality of Ni(II)/Pb(II)-Salen complex with SCN^- spacers: Insights from experimental and theoretical rationalization, *Inorg. Chem. Commun.*, 2024, **162**, 112155.

23 D. J. Majumdar, S. Roy and A. Frontera, The importance of tetrel bonding interactions with carbon in two arrestive iso-structural Cd(ii)–Salen coordination complexes: a comprehensive DFT overview in crystal engineering, *RSC Adv.*, 2022, **12**(55), 35860–35872.

24 S. Jana, P. K. Bhaumik, K. Harms and S. Chattopadhyay, Synthesis, characterization and DFT study of nickel(II) complexes of a N_2O donor Schiff base with different pseudo-halides: Formation of supra-molecular architectures by C–H$\cdots\pi$ interactions, *Polyhedron*, 2014, **78**, 94–103.

25 N. Sarkar, P. K. Bhaumik and S. Chattopadhyay, Manganese(III) complexes with tetradentate salicylaldimine Schiff bases: Synthesis, structure, self-assembly and catalase activity, *Polyhedron*, 2016, **115**, 37–46.

26 B. Dey, J. Cirera, S. Mehta, L. P. Ferreira, R. Arumugam, A. Mondal, P. N. Martinho and V. Chandrasekhar, Steric Effects on Spin States in a Series of Fe(III) Complexes, *Cryst. Growth Des.*, 2023, **23**, 6668–6678.

27 P. Chakraborty, S. Majumder, S. Jana and S. S. Mohanta, Syntheses, structures, catecholase activity, spectroscopy and electrochemistry of a series of manganese(III) complexes: Role of auxiliary anionic ligand on catecholase activity, *Inorg. Chim. Acta*, 2014, **410**, 65–75.

28 S. Roy, A. Bauzá, A. Frontera and S. Chattopadhyay, A combined experimental and theoretical study on two new di-nuclear cadmium(II) Schiff base complexes with selenocyanate-κ-Se, *Inorg. Chim. Acta*, 2016, **453**, 51–61.

29 C. R. Choudhury, S. K. Dey, N. Mondal, S. Mitra and V. Gramlich, Synthesis and structural studies of selenocyanato-bridged polymeric and molecular complexes of cadmium (II): presence of both end-to-end and end-on coordination, *Inorg. Chim. Acta*, 2003, **353**, 217–222.

30 I. Jess, J. Boeckmann and C. Nather, New cadmium thio- and selenocyanato coordination compounds: Structural snapshots on the reaction pathway to more condensed anionic networks, *Dalton Trans.*, 2012, **41**, 228–236.

31 A. Solanki and S. B. Kumar, Syntheses and structural studies of cobalt(II), nickel(II), zinc(II) and cadmium(II) selenocyanate complexes with a tetradentate N_4-donor ligand, *Polyhedron*, 2014, **81**, 323–328.

32 A. Kushwaha, D. Srivastava, G. Kociok-Köhn, S. Ahmed, E. R. T. Tiekink and A. Kumar, On the nature and interplay of Hg$\cdots$O/S spodium bonding and O$\cdots$S chalcogen bonding in one-dimensional phenylmercury(ii) 3-alkoxycyclobutene-1,2-dione-4-thiolate coordination polymers, *CrystEngComm*, 2025, **27**, 64–80.

33 P. Hobza, and K. Müller-Dethlefs, Noncovalent interactions: Theory and Experiment, in *RSC Theoretical and Computational Chemistry Series*, Royal Society of Chemistry, Cambridge, UK, 2010.

34 S. Scheiner, *Nonocovalent Forces*, Springer, Cham, Switzerland, 2015.

35 R. Tian, Y. Zeng, X. Li and X. Zhang, The nature of π-hole spodium bonds in the $HgLCl_2$ (L = pyrrole, pyrazole, imidazole, pyridine, pyridazine, and pyrimidine) complexes: from noncovalent to covalent interactions, *New J. Chem.*, 2024, **48**, 6582–6589.

36 S. Hazra, D. J. Majumdar, A. Frontera, S. Roy, G. Bouzid, H. Ghala and S. Dalai, On the Significant Importance of Hg$\cdots$Cl Spodium Bonding/σ/π-Hole/Noncovalent Interactions and Nanoelectronic/Conductivity Applications in Mercury Complexes: Insights from DFT Spectrum, *Cryst. Growth Des.*, 2024, **24**, 7246–7261.

37 D. J. Majumdar, A. Frontera, S. Roy and D. Sutradhar, Experimental and Theoretical Survey of Intramolecular Spodium Bonds/σ/π-Holes and Noncovalent Interactions in Trinuclear Zn(II)-Salen Type Complex with OCN^- Ions: A Holistic View in Crystal Engineering, *ACS Omega*, 2024, **9**, 1786–1797.

38 R. M. Gomila, A. Frontera and E. R. T. Tiekink, Supramolecular aggregation featuring Hg$\cdots$S secondary-bonding interactions in crystals of mercury(ii) species augmented by computational chemistry calculations, *CrystEngComm*, 2023, **25**, 5262–5285.

39 Q. Wu, S. A. C. McDowell and Q. Li, Single electron spodium bonds: Substituent effects, *Appl. Organomet. Chem.*, 2023, **37**, e7052.

40 W. Ruankham, N. Songtawee, V. Prachayasittikul, A. Worachartcheewan, W. Suwanjang, R. Pingaew, V. Prachayasittikul, S. Prachayasittikul and K. Phopin, Promising 8-Aminoquinoline-Based Metal Complexes in the Modulation of SIRT1/3-FOXO3a Axis against Oxidative Damage-Induced Preclinical Neurons, *ACS Omega*, 2023, **8**, 46977–46988.

41 (*a*) J. Chakraborty, S. Thakurta, B. Samanta, A. Ray, G. Pilet, S. R. Batten, P. S. Jensen and S. Mitra, Synthesis, characterisation and crystal structures of three trinuclear cadmium(II) complexes with multidentate Schiff base ligands, *Polyhedron*, 2007, **26**, 5139–5149; (*b*) *SMART & SAINT Software Reference Manuals Version 6.45*, Bruker Analytical X-ray Systems, Inc., Madison, WI, 2003; (*c*) *SHELXTL Reference Manual Ver. 6.1*, Bruker Analytical X-ray Systems, Inc., Madison, WI, 2000; (*d*) O. V. Dolomanov, L. J. Bourhis, R. J. Gildea, J. A. K. Howard and H. Puschmann, OLEX2: a complete structure solution, refinement and analysis program, *J. Appl. Crystallogr.*, 2009, **42**, 339–341; (*e*) G. M. Sheldrick, A Short History of SHELX, *Acta Crystallogr., Sect. A*, 2008, **64**, 112; (*f*) G. M. Sheldrick, *SHELXTL, a Software for Empirical Absorption Correction Ver.6.12*, Bruker AXS Inc., Madison, WI, 2001.

42 S. Grimme, Semiempirical hybrid density functional with perturbative second-order correlation, *J. Chem. Phys.*, 2006, **124**, 034108.
43 S. Grimme, J. Antony, S. Ehrlich and H. Krieg, A consistent and accurate *ab initio* parametrization of density functional dispersion correction (DFT-D) for the 94 elements H-Pu, *J. Chem. Phys.*, 2010, **132**, 154104.
44 C. Mchiri, B. Gassoumi, S. Acherar, M. A. M. Sh. El-Sharief and H. Nasri, Synthesis, X-ray molecular structure and QTAIM and NCI-RDG theoretic studies of a new cadmium (II) (4′4 diaminodiphenylmethane) (*meso*-arylporphyrin) coordination compound, *Inorg. Chem. Commun.*, 2021, **133**, 108924.
45 C. Mchiri, B. Gassoumi, H. Ghalla, S. Acherar, I. Turowska-Tyrke, A. Y. A. lzahrani, S. B. Moussa and H. Nasri, New cadmium(II) porphyrin-based coordination dimer: Experimental and theoretical studies, *J. Solid State Chem.*, 2022, **314**, 123364.
46 D. J. Majumdar, B. Gassoumi, A. Dey, S. Roy, S. Ayachi, S. Hazra and S. Dalai, Synthesis, characterization, crystal structure, and fabrication of photosensitive Schottky device of a binuclear Cu(II)-Salen complex: A DFT investigations, *RSC Adv.*, 2024, **14**, 14992–15007.
47 M. J. Frisch, G. W. Trucks, H. B. Schlegel, G. E. Scuseria, M. Robb, J. R. Cheeseman, G. V. Scalmani, V. Barone, G. A. Petersson, and H. Nakatsuji, *Gaussian 16, Revision A. 03*, Gaussian, Inc., Wallingford CT 32016.
48 D. Jayatilaka, S. K. Wolff, D. J. Grimwood, J. J. McKinnon and M. A. Spackman, CrystalExplorer: A Tool for Displaying Hirshfeld Surfaces and Visualising Intermolecular Interactions in Molecular Crystals, *Acta Crystallogr., Sect. A:Found. Crystallogr.*, 2006, **62**, 90.
49 D. J. Majumdar, J. E. Philip, B. Gassoumi, S. Ayachi, B. Abdelaziz, B. Tüzün and S. Roy, Supramolecular clumps of μ_2-1,3-acetate bridges of Cd(II)-Salen complex: Synthesis, spectroscopic characterization, crystal structure, DFT quantization's, and antifungal photodynamic therapy, *Heliyon*, 2024, **10**, e29856.
50 R. Ahlrichs, M. Bär, M. Häser, H. Horn and C. Kölmel, Electronic structure calculations on workstation computers: The program system turbomole, *Chem. Phys. Lett.*, 1989, **162**, 165–169.
51 C. Adamo and V. Barone, Toward reliable density functional methods without adjustable parameters: The PBE0 model, *J. Chem. Phys.*, 1999, **110**, 6158–6170.
52 E. Caldeweyher, S. Ehlert, A. Hansen, H. Neugebauer, S. Spicher, C. Bannwarth and S. Grimme, A generally applicable atomic-charge dependent London dispersion correction, *J. Chem. Phys.*, 2019, **150**, 154122.
53 F. Weigend, Accurate Coulomb-fitting basis sets for H to Rn, *Phys. Chem. Chem. Phys.*, 2006, **8**, 1057–1065.
54 (*a*) F. Weigend and R. Ahlrichs, Balanced basis sets of split valence triple zeta valence and quadruple zeta valence quality for H to Rn: Design and assessment of accuracy, *Phys. Chem. Chem. Phys.*, 2005, **7**, 3297–3305; (*b*) G. Mahmoudi, S. E. Lawrence, J. Cisterna, A. Cárdenas, I. Brito, A. Frontera and D. A. Safin, A new spodium bond driven coordination polymer constructed from mercury(ii) azide and 1,2-bis(pyridin-2-ylmethylene) hydrazine, *New J. Chem.*, 2020, **44**, 21100–21107; (*c*) V. Alizadeh, G. Mahmoudi, E. Priola, S. K. Seth, J. M. White, A. Frontera and D. A. Safin, Helical coordination complex of $Hg(ClO_4)_2$ with bulky hydrazone derivative: A Möbius-like discrete metal chelates, *Inorg. Chem. Commun.*, 2023, **149**, 110393; (*d*) R. Dennington, T. A. Keith, and J. M. Millam, *GaussView, Version 6.1*, Semichem Inc., Shawnee Mission, KS, 2016.
55 W. Humphrey, A. Dalke and K. Schulten, VMD: visual molecular dynamics, *J. Mol. Graph.*, 1996, **14**, 33–38.
56 R. F. W. Bader, A Quantum Theory of Molecular Structure and Its Applications, *Chem. Rev.*, 1991, **91**, 893–928.
57 J. Contreras-García, E. R. Johnson, S. Keinan, R. Chaudret, J.-P. Piquemal, D. N. Beratan and W. Wang, NCIPLOT: a program for plotting non-covalent interaction regions, *J. Chem. Theory Comput.*, 2011, **7**, 625–632.
58 T. Lu and F. Chen, Multiwfn: A multifunctional wavefunction analyzer, *J. Comput. Chem.*, 2012, **33**, 580–592.
59 E. D. Glendening, J. K. Badenhoop, A. E. Reed, J. E. Carpenter, J. A. Bohmann, C. M. Morales, P. Karafiloglou, C. R. Landis, and F. Weinhold, *NBO 7.0*, Theoretical Chemistry Institute, University of Wisconsin, Madison, WI, 2018.
60 K. Kitaura and K. Morokuma, A new energy decomposition scheme for molecular interactions within the Hartree-Fock approximation, *Int. J. Quantum Chem.*, 1976, **10**, 325–340.
61 I. Grabchev, E. Vasileva-Tonkova, D. Staneva, P. Bosch, R. Kukeva and R. Stoyanova, Impact of Cu(ii) and Zn(ii) ions on the functional properties of new PAMAM Metallo dendrimers, *New J. Chem.*, 2018, **42**, 7853–7862.
62 (*a*) M. A. Malik, O. A. Dar, P. Gull, M. Y. Wani and A. A. HAshmi, Heterocyclic Schiff base transition metal complexes in antimicrobial and anticancer chemotherapy, *Med. Chem. Commun.*, 2018, **9**, 409–436; (*b*) N. G. Heatley, A method for the assay of penicillin, *Biochem. J.*, 1944, **38**, 61–65; (*c*) D. S. Sarker, L. Nahar and Y. Kumarasamy, Microtitre plate-based antibacterial assay incorporating resazurin as an indicator of cell growth, and its application in the *in vitro* antibacterial screening of phytochemicals, *Methods*, 2007, **42**, 321–324.
63 K. D. Mjos, J. F. Cawthray, E. Polishchuk, M. J. Abrams and C. Orvig, Gallium(iii) and iron(iii) complexes of quinolone antimicrobials, *Dalton Trans.*, 2016, **45**, 13146–13160.
64 M. Balouiri, M. Sadiki and S. K. Bensouda, Methods for *in vitro* evaluating antimicrobial activity: A review, *J. Pharm. Anal.*, 2016, **6**, 71–79.
65 C. Wang, P. Wu, X.-L. Shen, X.-Y. Wei and Z.-H. Jiang, Synthesis, cytotoxic activity and drug combination study of tertiary amine derivatives of 2,4′-dihydroxyl-6′-methoxyl-3′,5′-dimethylchalcone, *RSC Adv.*, 2017, **7**, 48031–48038.
66 (*a*) J. Li, J. H. Huang, J. Y. G. Wang, Z. Z. Chen and J. Lei, An intramolecular hydrogen bond-promoted "green" Ugi cascade reaction for the synthesis of 2,5-diketopiperazines with anticancer activity, *RSC Adv.*, 2022, **12**, 33175–33179; (*b*) M. F. Maria, C. Fornasiero and A. M. Isetta, *J. Immunol.*

Methods, 1990, **131**, 165–172; (*c*) R. G. Dulbecco and G. Freeman, Plaque production by the polyoma virus, *Virology*, 1959, **8**, 396–397; (*d*) A. Kumar and J. Ameeramja, Chapter 2 - Cell viability and apoptotic assays to assess drug efficacy, *Protoc. Handb. Cancer Biol.*, 2021, 7–22.

67 K. Priya, M. Vijayakumar and B. Janani, Chitosan-mediated synthesis of biogenic silver nanoparticles (AgNPs), nanoparticle characterisation and *in vitro* assessment of anticancer activity in human hepatocellular, *Int. J. Biol. Macromol.*, 2020, **149**, 844–852.

68 S. Hazra, D. J. Majumdar, J. E. Philip, G. Bouzid, H. Ghalla, S. Roy and S. Dalai, Dicyanamide Anion Protracted Assemblies of Cd(II)-Salen Type Coordination Polymers: Synthetic Perspective, Characterization, Crystallographic Notability, DFT Overview, and Biological Appraisal, *J. Inorg. Organomet. Polym.*, 2024, **35**, 661–679.

69 D. J. Majumdar, J. E. Philip, B. Tuzun and S. Roy, Synthesis, characterization, crystallographic aspects, Fukui function, and photodynamic antifungal chemotherapy investigation of Cd(II)-tricyanomethanide coordination polymer: Insights from DFT, *Inorg. Chem. Commun.*, 2023, **155**, 111057.

70 (*a*) R. Wang, Y. Cao, D. Jia, L. Liu and F. Li, New approach to synthesize 8-hydroxyquinoline-based complexes with Zn^{2+} and their luminescent properties, *Opt. Mater.*, 2013, **36**, 232–237; (*b*) X. H. Wang, M. W. Shao and L. Liu, Photoconductivity of a bundle of Bis(8-hydroxyquinoline) cadmium nanoribbons, *J. Mater. Sci.: Mater. Electron.*, 2011, **22**, 120–123.

71 M. Tunçel and S. Serin, Synthesis and characterization of copper(II), nickel(II) and cobalt(II) complexes with azo-linked Schiff base ligands, *Synth. React. Inorg. Metal-Org. Nano-Metal Chem.*, 2005, **35**, 203–212.

72 B. Dutta, S. Paul and S. Halder, Explosive and pollutant nitroaromatic sensing through a Cd(II) based ladder shaped 1D coordination polymer, *Heliyon*, 2023, **9**, e13504.

73 J. Luo, Q. Niu, M. Jin, Y. Cao, L. Ye and R. Du, Study on the effects of oxygen-containing functional groups on Hg adsorption in simulated flue gas by XAFS and XPS analysis, *J. Hazard. Mater.*, 2019, **376**, 21–28.

74 S. Hazra, D. J. Majumdar, J. E. Philip, G. Bouzid, A. Frontera, S. Roy, H. Ghalla and S. Dalai, 8-Aminoquinoline-Based Promising Zn Complexes with Dicyanamide and Tricyanomethane Anions: Supramolecular $R_4^4(8)/R_2^2(16)$ Synthons, DFT Rationalization, and Biological Insights, *ACS Omega*, 2025, **10**, 14770–14786.

75 (*a*) H. Wang, M. Thangamuthu, Z. Wu, J. Yang, H. Yuan, M. K. Bayazit and J. Tang, Self-assembled sulphur doped carbon nitride for photocatalytic water reforming of methanol, *Chem. Eng. J.*, 2022, **445**, 136790; (*b*) A. Singh, G. Kociok-Kohn, A. Dutta, A. Kumar and M. Muddassir, Diaminopyridine Hg(II)-based 1D supramolecular polymer: Crystallographic and computational insights into spodium bonding, *J. Solid State Chem.*, 2022, **315**, 123517; (*c*) G. Mahmoudi, A. Masoudiasl, M. G. Babashkina, A. Frontera, T. Doert, J. M. White, E. Zangrando, F. I. Zubkov, D. A. Safin and D. A, On the importance of π-hole spodium bonding in tricoordinated HgII complexes, *Dalton Trans.*, 2020, **49**, 17547–17551; (*d*) A. H. Sheikh, R. B. Choudhury, V. K. Deb, T. Shahnowaz, S. Mukherjee, K. Pramanick, W. Kaminsky, N. A. Choudhury, S. Roy, R. Shukla, A. V. Gurbanov, G. Mahmoudi and S. Adhikari, Insights into the spodium bonding characteristics of a bactericidal Hg(II) complex, *New J. Chem.*, 2025, **49**, 7900–7909; (*e*) A. Md. Asaduzzaman and G. Schreckenbach, Chalcogenophilicity of Mercury, *Inorg. Chem.*, 2011, **50**, 3791–3798; (*f*) A. A. Tehrani, H. Ghasempour, A. Morsali, A. Bauzá, A. Frontera and P. Retailleau, Unraveling the dual character of sulfur atoms in a series of Hg (ii) coordination polymers containing bis (4-pyridyl) disulfide, *CrystEngComm*, 2017, **19**, 1974–1981; (*g*) T. S. Lobana, R. Verma, A. Singh, M. M. Shikha and A. Castineiras, Metal-phosphine chalcogenide interactions.Crystal structures of palladium(II)/mercury(II) complexes with 1,2-bis(diphenylthiophosphinyl)ethane containing seven-membered metallacyclic rings, *Polyhedron*, 2002, **21**, 205–209.

76 B. Gassoumi, A. M. Mahmoud, S. Nasr, A. Karayel, S. Özkınalı, M. E. Castro, F. J. Melendez, M. Mahdouani, L. Nouar, F. Madi, H. Ghalla, R. Bourguiga, R. B. Chaabane and Y. Zhou, Revealing the effect of Co/Cu (d7/d9) cationic doping on an electronic acceptor ZnO nanocage surface for the adsorption of citric acid, vinyl alcohol, and sulfamethoxazole, *Mater. Chem. Phys.*, 2023, **309**, 128364.

77 (*a*) H. Hadi, B. Gassoumi, S. Nasr, R. Safari, A. A. Basha, P. M. Imran, H. Ghalla, M. T. Caccamo and S. Ayachi, Design, Transport/Molecular Scale Electronics, Electric Properties, and a Conventional Quantum Study of a New Potential Molecular Switch for Nanoelectronic Devices, *ACS Omega*, 2024, **9**, 1029–1041; (*b*) N. Blankevoort, P. Bastante, R. J. Davidson, R. J. Salthouse, A. H. S. Daaoub, P. Cea, S. M. Solans, A. S. Batsanov, S. Sangtarash, M. R. Bryce, N. Agrait and H. Sadeghi, Exploring the Impact of the HOMO–LUMO Gap on Molecular Thermoelectric Properties: A Comparative Study of Conjugated Aromatic, Quinoidal, and Donor–Acceptor Core Systems, *ACS Omega*, 2024, **9**(7), 8471–8477.

78 M. Dhifet, B. Gassoumi, N. Issaoui and H. Nasri, Bis(2,3,5,6-tetrafluorothiophenolato) Iron(III) (α,α,α,β)-Tetrakis(*o*-pivalamidophenyl) porphyrin Ion Complex: Synthesis, Spectroscopic, Structural Characterization and Computational Studies, *ChemistrySelect*, 2024, **9**, e202401491.

79 B. Abdelaziz, Z. Mazouz, B. Gassoumi, N. E. I. Boukortt and S. Ayachi, Molecular engineering of D-π-A-type structures based on nitrobenzofurazan (NBD) derivatives for both organic solar cells and nonlinear optical response, *J. Mol. Liq.*, 2024, **395**, 123934.

80 P. Pritha, G. Kishore, S. Xavier, F. Paularokiadoss, D. Bhakiaraj, S. Periandy, G. Bouzid and S. Ayachi, Sunlight-activated dye degradation of ZnO/CdO-decorated graphene oxide and its antibacterial activity, *Mater. Chem. Phys.*, 2024, **326**, 129829.

81 (*a*) T. Damena, M. B. Alem, D. Zeleke and T. Desalegn, Synthesis, characterization, and biological activities of zinc(II), copper(II) and nickel(II) complexes of an aminoquinoline derivative, *Front. Chem.*, 2022, 1053532; (*b*) A. M. Montaña and C. Batalla, The rational design of anticancer platinum complexes: the importance of the structure-activity relationship, *Curr. Med. Chem.*, 2009, **16**, 2235–2260; (*c*) C. M. Meléndez, G. A. Barraza, F. Sojo, F. Arvelo and V. V. Kouznetsov, Substituted 2-arylquinoline and 2-methyl-1,2,3,4-tetrahydroquinoline derivatives with selective anticancer activity: synthesis, structure–activity relationships, and molecular modelling insights, *New J. Chem.*, 2024, **48**, 19674–19690.

82 (*a*) CCDC 2440026: Experimental Crystal Structure Determination, 2025, DOI: 10.5517/ccdc.csd.cc2mx1j4; (*b*) CCDC 2440027: Experimental Crystal Structure Determination, 2025, DOI: 10.5517/ccdc.csd.cc2mx1k5.